
Covariant spatio-temporal receptive fields for spiking neural networks

J. E. Pedersen, J. Conradt and T. Lindeberg

Computational Science and Technology

KTH Royal Institute of Technology

Stockholm

{jeped@kth.se}

ABSTRACT

Biological nervous systems constitute important sources of inspiration towards computers that are faster, cheaper, and more energy efficient. Neuromorphic disciplines view the brain as a coevolved system, simultaneously optimizing the hardware and the algorithms running on it. There are clear efficiency gains when bringing the computations into a physical substrate, but we presently lack theories to guide efficient implementations. Here, we present a principled computational model for neuromorphic systems in terms of spatio-temporal receptive fields, based on affine Gaussian kernels over space and leaky-integrator and leaky integrate-and-fire models over time. Our theory is provably covariant to spatial affine and temporal scaling transformations, and with close similarities to visual processing in mammalian brains. We use these spatio-temporal receptive fields as a prior in an event-based vision task, and show that this improves the training of spiking networks, which otherwise is known as problematic for event-based vision. This work combines efforts within scale-space theory and computational neuroscience to identify theoretically well-founded ways to process spatio-temporal signals in neuromorphic systems. Our contributions are immediately relevant for signal processing and event-based vision, and can be extended to other processing tasks over space and time, such as memory and control.

Keywords Scale-space theory · Neuromorphic computing · Computer vision

1 Introduction

Brain-inspired *neuromorphic* algorithms and hardware are heralded as a possible successor to current computational devices and algorithms [Mead, 2023, Schuman et al., 2022]. Mathematical models that approximate biological neuron dynamics are known for their computational expressivity [Maass, 1997] and neuromorphic chips have shown to operate faster and with much less energy than computers based on the von Neumann architecture [Mead, 2023]. These “biomimetic” neural systems are decentralized and sparsely connected, which renders most sequential algorithms designed for present computers intractable. A few classical algorithmic problems have successfully been recast to neuromorphic hardware, such as MAXCUT [Theilman and Aimone, 2023] and signal demodulation [Arnold et al., 2023], but no neuromorphic algorithm or application has, yet, been able to perform better than digital deep learning techniques [Schuman et al., 2022]. Before we can expect to exploit the possible advantages of neuromorphic systems, we must first discover a theory that accurately describe these systems with a similar precision as we have seen for digital computations [Aimone and Parekh, 2023]. Without such a theoretical framework, neuromorphic systems will routinely be outperformed by dense and digital deep learning models [Tayarani-Najaran and Schmuker, 2021].

Scale-space theory studies signals across scales [Koenderink, 1984] and has been widely applied in computer vision [Lindeberg, 1994], and, recently, deep learning [Jacobsen et al., 2016, Worrall and Welling, 2019, Lindeberg, 2022]. Lindeberg presented a computational theory for visual receptive fields that leverages symmetry properties over space and time [Lindeberg, 2013], which is appealing from two perspectives: it provides a *normative* view on visual processing that is remarkably close to the stages of visual processing in higher mammals [Lindeberg, 2021], and it provably captures natural image transformations over space and time [Lindeberg, 2023a]. Scale-space theory is

closely tied to covariance (or equivariance) which is a desirable property, because it optimally encodes and generalizes transformations in the feature space. Covariance have gained popularity in the machine learning literature [Cohen and M. Welling, 2016] and examples are abundant in classical computer vision, where scale invariance and covariance for image and video data under varying image transformations have been proposed, including objects of different size in purely spatial images [Lindeberg, 1998, Mikolajczyk and Schmid, 2004, Lowe, 2004, Lindeberg, 2015], objects varying in projected image size due to depth variations over time [Bretzner and Lindeberg, 1998], or objects and events under simultaneous spatial and temporal scaling variations [Lindeberg, 2016, Lindeberg, 2018, Jansson and Lindeberg, 2018]. However, there have not been any previously reported treatments of scale-space for event-based vision or joint spatio-temporal scale channels for deep learning on video data.

This work sets out to improve our understanding of spatio-temporal computation for event-based vision from first principles, with an emphasis on theoretically optimal encodings of objects under spatial and temporal transformations. We study the idealized computation of spatio-temporal signals through the lens of scale-space theory and establish covariance properties under spatial and temporal image transformations for biologically inspired neuron models (leaky integrate and leaky integrate-and-fire). Applying our findings to an object tracking task based on sparse, simulated event-based stimuli, we find that our approach benefits from the idealized covariance properties and significantly outperforms naïve deep learning approaches.

Our main contribution is a computational model that provides falsifiable predictions for event-driven spatio-temporal computation. We additionally provide experimental evidence that demonstrates the benefits of our approach in several event-based object tracking tasks. While we primarily focus on event-based vision and signal processing, we discuss more general applications within memory and closed-loop neuromorphic systems with relevance to the wider neuromorphic community.

Specifically, we contribute with (a) biophysically realizable neural primitives that are covariant to spatial affine transformations, Galilean transformations as well as temporal scaling transformations, (b) a normative model for event-driven spatio-temporal computation, and (c) an implementation of stateful biophysical models that perform better than stateless artificial neural networks in an event-based vision regression task.

Related work

Scale-space theory

Representing signals at varying scales was studied in modern science in the 70's [Uhr, 1972, Koenderink and van Doorn, 1976] and formalized in the 80's and 90's [Koenderink, 1984, Lindeberg, 1994]. Specifically, scale spaces were introduced by Witkin in 1983, who demonstrated how signals can be processed over a continuum of scales [Witkin, 1987]. In 1984, Koenderink introduced the notion that images could be represented as functions over three "coordinate" variables $L : \mathbb{R}^2 \times \mathbb{R}_+ \rightarrow \mathbb{R}$, where a scale parameter represents the evolution of a diffusion process over the image domain [Koenderink, 1984]. Operating with diffusion processes, represented as Gaussian kernels, is particularly attractive because they parameterize scaling operations in the image plane as a linear operation [Lindeberg, 1994]. In turn, this permits a concise and correct description of transformation in the signal plane which has successfully been leveraged in algorithms for computer vision. For instance in the early convolutional networks [Bretzner and Lindeberg, 1998, Lecun et al., 1998], but also in recent deep learning papers under the name *equivariance* with extension to other transformations than scaling under the guise of group theory. Specifically, they consider group actions under certain symmetric constraints, such as the circle $\mathbb{S}^1 \simeq \text{SO}(2)$ [Cohen and M. Welling, 2016, Worrall and Welling, 2019, Bekkers, 2020]. Related to scale-space theory, Lindeberg introduced covariance properties for more general spatial transformations [Lindeberg, 2013], and Howard et al. [Howard et al., 2023] revisited temporal reinforcement learning and identified temporal scale covariance in time-dependent deep networks as a fundamental design goal. Finally, we refer the reader to a large body of literature that studies general covariance properties for stochastic processes [Porcu et al., 2021].

Computational models of neural circuits

Mathematical models of the electrical properties in nerves date back to the beginning of the 20th century, when Luis Lapicque approximated tissue dynamics as a leaky capacitor [Blair, 1932]. The earliest studies of computational models appear in Lettvin *et al.* [Lettvin et al., 1959], who identified several visual *operations* performed on the image of a frog's brain, and in Hubel and Wiesel's [Hubel and Wiesel, 1962] demonstration of clear tuning effects of visual receptive fields in cats, which allowed them to posit concrete hypotheses about the functional architecture of the visual cortex. Many postulates have been made to formalize computations in neural circuits since then, but studying computation in individual circuits has only "been successful at explaining some (relatively small) circuits and certain hard-wired behaviors" [Richards et al., 2019, p. 1768]. We simply do not have a

good understanding of the spatio-temporal computational principles under which biophysical neural systems operate [Aimone and Parekh, 2023, Mead, 2023, Tayarani-Najaran and Schmuker, 2021].

The notion of scale-space theory relates directly to sensory processing in biology, where multiple distributed time-scales are known to play a critical role [Lettvin et al., 1959, Miri et al.,]. For instance, in time-invariant dynamics of neural memory representations [Howard et al., 2023] and the spatial components of visual receptive fields [Lindeberg, 2013, Lindeberg, 2021]. Additionally, [Perez-Nieves et al., 2021] demonstrated that heterogeneous time constants metabolically efficient way to represent multiple time scales, particularly if they are tuned to the time scales in the tasks. More recently, scale-space theory has been enhanced the performance of deep convolutional neural networks significantly [Evans et al., 2022] while enabling invariance to time-scaling operations [Jacques et al., 2022]. Applying banks of Gaussian derivative fields, as arising from scale-space theory, has been demonstrated to express provably scale-covariant and scale-invariant deep networks [Lindeberg, 2022].

Event-based vision

Inspired by biological retinas, the first silicon retina was built in 1970 [Fukushima et al., 1970] and independently by Mead and Mahowald in the late 1980s [Mead, 1989]. Event-based cameras have since then been studied and applied to multiple different tasks [Gallego et al., 2022, Tayarani-Najaran and Schmuker, 2021], ranging from low-level computer vision tasks such as feature detection and tracking [Litzenberger et al., 2006, Ni et al., 2012] to more complex applications like object segmentation [Barranco et al., 2015], neuromorphic control [Delbrück and Lang, 2013], and recognition [Ghosh et al., 2014].

In 2011, Folowosele *et al.* [Folowosele et al., 2011] applied receptive fields and spiking neural networks to perform visual object recognition. In 2014, Zhao *et al.* [Zhao et al., 2015] introduced “cortex-like” Gabor filters in a convolutional architecture to classify event-based motion detection, closely followed by Orchard *et al.* [Orchard et al., 2015]. In 2017, Lagorce *et al.* [Lagorce et al., 2017] formalized the notion of spatial and temporal features in spatio-temporal “time surfaces” which they composed in hierarchies to capture higher-order patterns. This method was extended the following year to include a memory of past events using an exponentially decaying factor [Sironi et al., 2018]. Schaefer *et al.* [Schaefer et al., 2022] used graph neural networks to parse subsampled, but asynchronous events in time windows. More recently, Nagaraj *et al.* [Nagaraj et al., 2023] contributed a method based on sparse, spatial clustering that differentiates events belonging to objects moving at different speeds.

2 Results

We establish spatio-temporal covariance for event-driven leaky integrator and leaky integrate-and-fire neuron models by extending the generalized Gaussian derivative model for spatio-temporal receptive fields [Lindeberg, 2016, Lindeberg, 2021]. To validate the theory, we later demonstrate by experiments that the spatio-temporal receptive fields, encoded with priors from the theory, provide a clear advantage compared to baseline models.

Joint covariance under geometric image transformations

Image data are subject to natural image transformations, which to first-order of approximation can be modelled as a combination of three types of geometric image transformations:

1. spatial affine transformations $x' = A x$, where A is an affine transformation matrix,
2. Galilean transformations $x' = x + u t$, where u is a velocity vector and t denotes time, and
3. temporal scaling transformations $t' = S_t t$, where S_t is a temporal scaling factor.

Scale-space theory prescribes that signals subject to the transformations above can be represented in a covariant way by a scale-space representation L [Lindeberg, 2021, Lindeberg, 2023a]. Additionally, we can know the exact transformations between two scale-space representations L and L' , provided that the parameters of the capturing mechanism are matched to the image transformation. That is, the image transformations and scale-space smoothing operations commute, as detailed in the Methods Section “Relationship under geometric image transformations” and Supplementary Materials Section B.

Figure 1 illustrates 4×4 spatio-temporal receptive fields that are initialized to capture signals that have been scaled over space and time. The horizontal axes in the plots represent a 1-dimensional kernel that is scaled to match different spatial scales across the rows of the figure. The vertical axes represent the amount of temporal smoothing, which varies across the columns. By applying each receptive field to a given signal, we get the canonical scale-space representation at the given spatial and temporal scales.

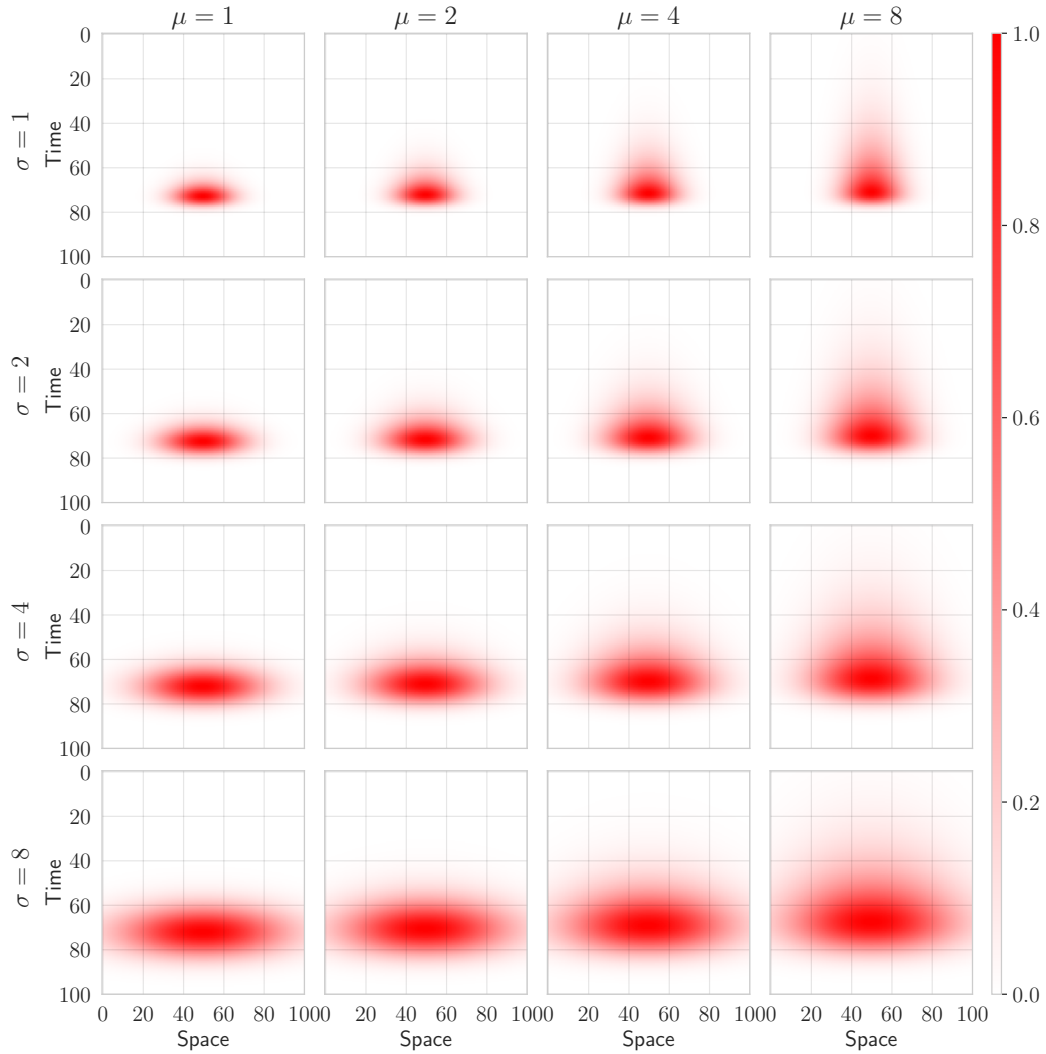


Figure 1: Spatio-temporal receptive fields parameterized over 4 spatial scales (σ) and 4 temporal scales (μ). By increasing the size of the receptive field (rows), the receptive fields become sensitive to larger spatial sizes. By increasing the temporal scale of the receptive fields (columns), the receptive fields become sensitive to larger temporal scales. The receptive fields in this figure have been normalized to $[0, 1]$.

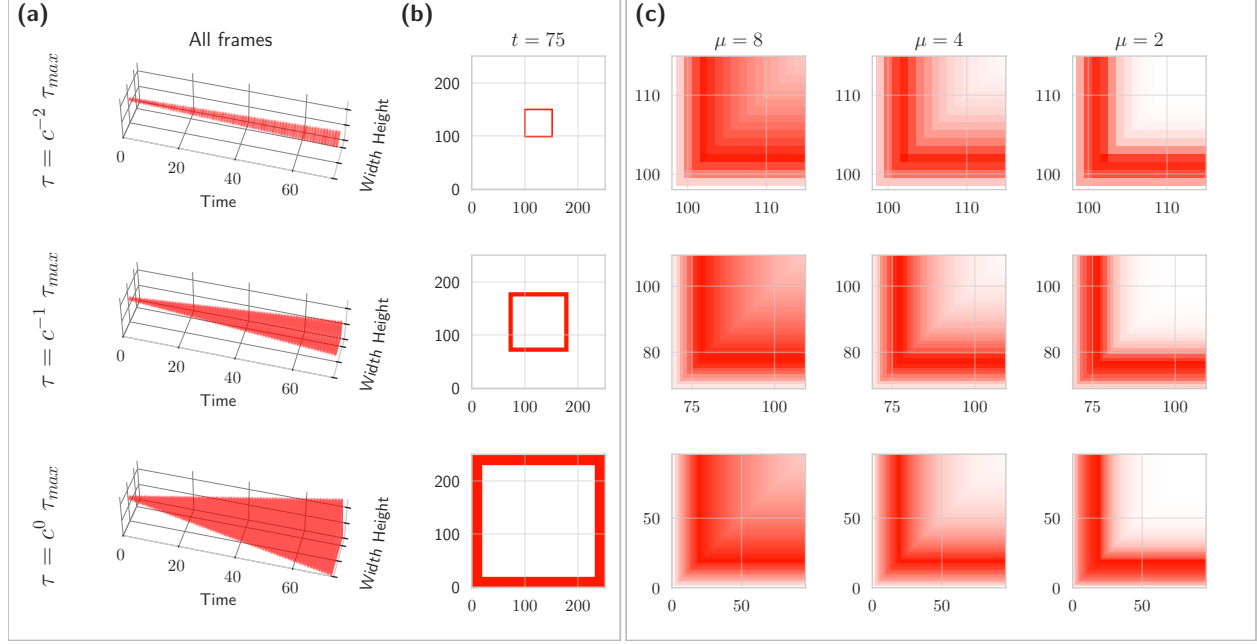


Figure 2: Illustration of the combined spatial and temporal scale covariance properties of the underlying spatio-temporal receptive field representation. When we scale three identical squares in at different scale velocities τ over 75 timesteps in panel (a), according to Equation 16, we observe a large variance in the scale at the final timestep $t = 75$ in panel (b). Panel (c) shows the receptive field responses of the stimulus in (a) for different temporal scale parameters μ in panel. The responses appear similar, but occur at largely different spatial scales, because the spatial scale velocities τ are matched to the parameters of the geometric image transformations. In the ideal continuous case they would be identical.

To be sensitive to the spatial and the temporal scales in any given data distribution, care must be taken to sample the parameter space accordingly. To explicitly handle variable spatial and temporal scales in the event-based video data, we filter the input data with a distribution of spatial receptive fields over a set of different spatial scales, that are in turn also expanded over 4 temporal scales, as detailed in the Methods Section on “Model architecture and training”

The commutative relationship between scale-space smoothing operations and natural image transformations enables us to capture fundamental spatio-temporal video transformations. This theoretical foundation permits us to model how visual information changes across both space and time (shown mathematically in Figure 6 of the Methods Section). Models must accurately reflect the underlying data distribution through properly calibrated spatial and temporal parameters. When these parameters are misaligned, the model fails to capture essential transformations in the data, effectively becoming “blind” to important changes.

This alignment between spatial and temporal receptive fields and the underlying data is critical for accurate visual processing. Figure 2 illustrates this joint covariance property through a case study of spatial and temporal scaling operations. The experiment tracks a 2-dimensional square (panels (a) and (b)) as it scales over 75 time steps at three different velocities (panel (a)). By $t = 75$, these varying velocities result in squares of significantly different sizes (panel (b)). Panel (c) reveals how spatio-temporal receptive fields respond covariantly to these scaled squares. Remarkably, despite substantial differences in square sizes, the outputs remain similar across scales. Different temporal scale factors (μ) produce functionally equivalent responses, regardless of whether scaling occurs in the input signal or evolves over time. This scale-matching property significantly enhances the performance of computer vision algorithms that utilize spatio-temporal receptive fields, as it aligns naturally with geometric image transformations. The result is a more robust and theoretically grounded approach to video analysis.

Temporal scale covariance for leaky integrators and leaky integrate-and-fire models

Under the image transformations above, we extend the notion of the temporal processing in the scale-space representations L and L' to leaky integrators and leaky integrate-and-fire models. When reduced to a purely temporal domain under a temporal scaling transformation of the form $t' = S_t t$, where $S_t > 0$ is the temporal scaling fac-

tor, a scale-covariant purely temporal scale-space representation should obey [Lindeberg, 2017, Eq. (10) for $n = 0$] [Lindeberg, 2023b, Eq. (23)]

$$L(t; \tau) = L'(t'; \tau') \quad (1)$$

where τ and $\tau' = S_t^2 \tau$ are matching temporal scale parameters. A specific type of temporal scale channel representation L for some signal f can be written as [Lindeberg and Fagerström, 1996, Eq. (14)]

$$L(t; \mu) = \int_0^\infty f(t-u) h_{exp}(\cdot; \mu) du, \quad (2)$$

where μ is a time constant and $h_{exp}(\xi; \mu) = \frac{1}{\mu} e^{-\xi/\mu}$. The leaky integrator can be understood as the integration of a decaying exponential function of some input signal I [Gerstner et al., 2014, Eq. (1.11)]

$$u(t; \mu) = \int_0^\infty \frac{1}{\mu} e^{-\xi/\mu} I(t-\xi) d\xi. \quad (3)$$

By reformulating f and h , we observe that the two temporal representations in Equations (20) and (21) are covariant under temporal scaling transformations. A full derivation is available in the Methods Section ‘‘Temporal scale covariance for leaky integrator models’’.

The leaky integrate-and-fire model expands the leaky integrator model with a Heaviside threshold, which causes the neuron to emit a spike and reset the temporally integrated value u to 0. Assuming that the membrane reset can be expressed as a rapid, but linear, decay, we can express the leaky integrate-and-fire model as a series of kernels according to the Spike Response Model (SRM) described in the Methods Section ‘‘Spike response model’’

$$z(t) = -\theta_{thr} e^{-(t-t_f)/\mu_r} + \int_0^\infty \kappa(s) I(t-s) ds, \quad (4)$$

where θ_{thr} is the threshold, μ_r is the reset time constant, and κ is the linear membrane filter. Under mild assumptions, we show that the leaky integrate-and-fire In the Methods Section ‘‘Temporal scale covariance for leaky integrate-and-fire models’’, we provide the full exposition of how we can make the leaky integrate-and-fire model covariant under temporal scaling transformations.

A main corollary of these results is that, by replacing the previous temporal smoothing kernels in the spatio-temporal receptive fields in the spatio-temporal scale-space representations [Lindeberg, 2016, Lindeberg, 2021, Lindeberg, 2023a] by either leaky integrators or leaky integrate-and-fire models, we can construct joint covariant spatio-temporal receptive fields in spiking neural networks, which can in theory exploit the symmetry properties of the underlying transformations that objects in event-based vision data are subject to.

Initializing deep networks with idealized receptive fields

It is well known that spiking neural networks are comparatively harder to train than non-spiking neural networks for event-based vision, and they are not yet comparable in performance to methods used for training non-spiking deep networks [Neftci et al., 2019, Schuman et al., 2022, Eshraghian et al., 2023]. To guide the training process for spiking networks, we propose to initiate the receptive fields with priors according to the idealized model for covariant spatio-temporal receptive fields. Following this idea, we used the purely spatial component of the spatio-temporal receptive fields by scale-normalized affine directional derivative kernels according to [Lindeberg, 2021, Equation (31) for $\gamma = 1$]

$$T_{\varphi^{m_1} \perp \varphi^{m_2}, norm}(x_1, x_2; \Sigma) = \sigma_\varphi^{m_1} \sigma_{\perp \varphi}^{m_2} \partial_\varphi^{m_1} \partial_{\perp \varphi}^{m_2} (g(x_1, x_2; s \Sigma)), \quad (5)$$

where

- $g(x_1, x_2; s \Sigma)$ is a Gaussian kernel with spatial scale parameter $s > 0$ and a positive definite covariance matrix Σ ,
- $\partial_\varphi = \cos \varphi \partial_{x_1} + \sin \varphi \partial_{x_2}$ and $\partial_{\perp \varphi} = -\sin \varphi \partial_{x_1} + \cos \varphi \partial_{x_2}$ denote directional derivatives in directions φ and $\perp \varphi$ parallel to the two eigendirections of the spatial covariance matrix Σ ,
- m_1 and m_2 denote the orders of spatial differentiation, and
- $\sigma_\varphi = \sqrt{\lambda_\varphi}$ and $\sigma_{\perp \varphi} = \sqrt{\lambda_{\perp \varphi}}$ denote spatial scale parameters in these directions, with λ_φ and $\lambda_{\perp \varphi}$ denoting the eigenvalues of the spatial covariance matrix Σ .

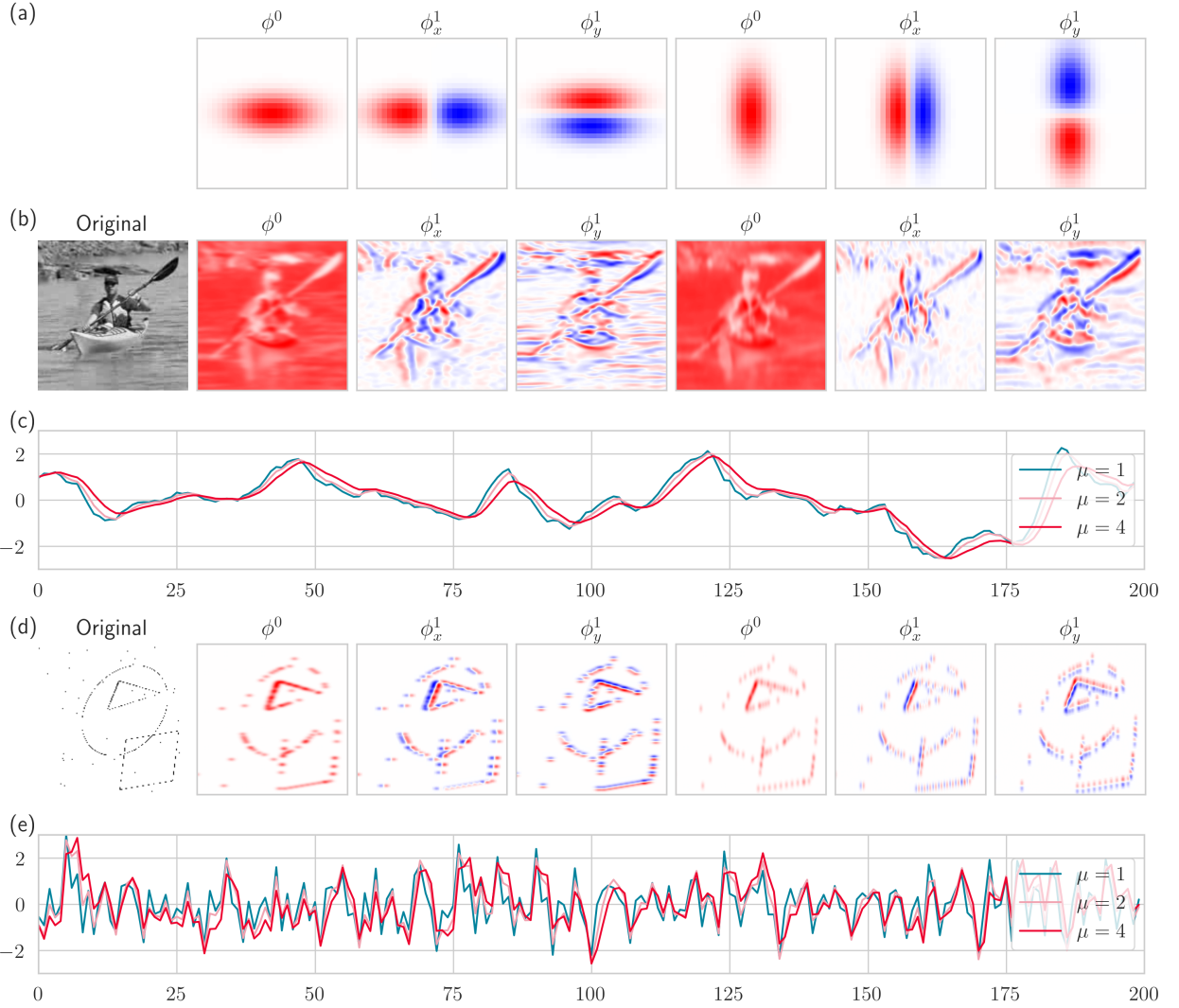


Figure 3: Illustrations of spatial-temporal receptive field responses to natural video and event-based video. (a): spatial receptive fields at angles 0° and 90° and their directional derivatives up to the first order. (b): a still frame from the UCF-101 dataset [Soomro et al., 2012] and the response for each of the kernels in (a) for $\mu = 1$. (c): averaged temporal traces from temporal receptive fields with three μ when applied to the UCF-101 video. (d): a still frame from our simulated event-based dataset and the response for each of the kernels in (a) for $\mu = 1$. (e): averaged temporal traces from temporal receptive fields with three μ when applied to the video from (d). The sparsity and noise in the event-based video results in a much more irregular response over time.

This receptive field model directly follows the spatial component in the covariant receptive field model detailed in the Section “Joint covariance under geometric image transformations”, while restricted to the special case when the image velocity parameter $v = 0$, and complemented with spatial differentiation, to make the receptive fields more selective. Receptive fields from this family have been demonstrated to be very similar to the receptive fields of simple cells in the primary visual cortex (see Figures 16 and 17 in [Lindeberg, 2021]). For the temporal scales, we initialize logarithmically distributed time constants in the interval $[1, 4]$ for the leaky integrate-and-fire neurons, as described in the Methods Section called Model architecture and training.

Figure 3 (a) visualizes a subset of the spatial receptive fields that we used in the experiments below along with responses to both frame-based and event-based video. The panels (b) and (d) visualize the results of convolving the spatial receptive fields with conventional image data and event data, respectively, and the panels (c) and (e) show how the temporal traces change according to the temporal scale. When the temporal scale increases, the delay increases and effectively smoothens out the signal. Striking a balance between the spatial and temporal scales is crucial for the model to be able to track the shapes in the event-based video data at appropriate temporal resolutions: too short temporal scales will produce imprecise and noisy predictions, while too long temporal scales will result in delayed and smeared-out responses.

Experimental results

We proceed by experimentally measuring the effect of the initialization scheme in an event-based object tracking task. We built a 3-layer convolutional model whose parameters are configured either according to our receptive field (RF) theory, or according to the default, uniform initialization scheme. Three kinds of activation functions are used: leaky integrators (LI), leaky integrate-and-fire (LIF) neurons, and stateless ReLU for a comparable baseline. Since LI and LIF models integrate signal over time and ReLU models do not, ReLU models are disadvantaged when processing temporal information such as sparse events. To compensate for the lack of state in ReLU models, we introduce a ReLU variant that operates on eight previous visual frames (multi-frame; MF), as opposed to the other single-frame (SF) models. This effectively provides the model with a temporal memory and cancel out much of the advantage of the LI and LIF models (see Section 4 for details).

Spatial and temporal scaling

Figure 4 shows the results when training our model to track sparse and event-based shapes subject to scaling transformations in space (left) and time (right) (see the “Methods” section “Dataset” for details on the task). Both in the spatial and temporal scaling scenarios, the effect of our initialization scheme is highly significant ($>= 1.9$) for the leaky integrator models (see Methods section “Initialization effect size” for details on the metric). The effect is still significant for the leaky integrate-and-fire model in the spatial case, but less it is pronounced than in the temporal scaling task. In general, the performance for the spatial task is higher, also in the other models, which indicates that the task overall is easier for the model to solve.

The initialization effect is less pronounced in the ReLU models. Since the gradient landscape is much simpler in ReLU models than spiking models [Kreutzer et al., 2020], backpropagation should find more optimal parameter distributions as training progresses. Despite that, the ReLU models fall behind in overall performance. The single frame (SF) model is likely struggling with the highly sparse signals, as shown in Figure 8, of which the model sees only a single frame per timestep. This is evidenced by the increased performance of the multi-frame model (MF), because the only difference to the SF model is the simultaneous exposure to eight frames extending backwards in time. Therefore, the increased performance must be due to the MF model’s ability to correlate signals across frames. Even with multiple frames, however, the ReLU models are clearly outperformed by the leaky-integrator or leaky integrate-and-fire models, neither of which integrate more than one frame per timestep.

We additionally plotted the distributions of the time constants μ during training for the leaky integrator models in Figure 4C for both initialization schemes. As expected, the RF initialization scheme provides a more stable distribution of time constants, even though the time constants are optimized with backpropagation through time, similar to all the other model parameters. The uniformly initialized time constants are more spread out, as expected, but appears to converge around similar time constants μ as the RF models, indicating that the initialized values are a good starting point. This is further confirmed if we look at the variance of μ relative to their initial values in Figure 4D, where the time constants in the uniform models are much more volatile as training progresses.

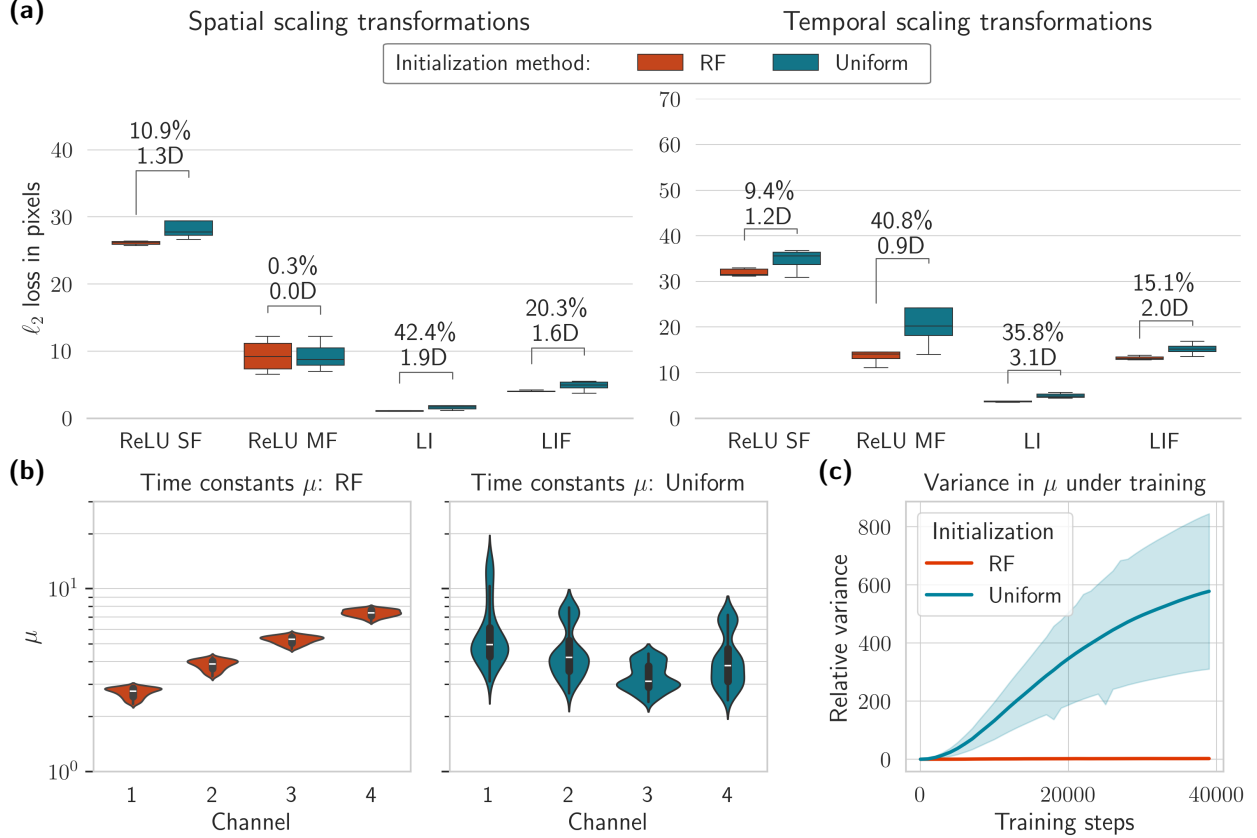


Figure 4: Experimental results for event-based shapes subject to spatial or temporal scaling transformations across 5 training runs. **(a)** Accuracy results for spatial (left) and temporal (right) scaling operations across four different models: ReLU single frame (SF), ReLU multi-frame (MF), leaky integrator (LI), and leaky integrate-and-fire (LIF). Each model is initialized either according to our receptive field theory (RF) or uniform white noise in the same parameter domain. The numbers above the distributions show the difference in performance in percentage and the effect size (Cohen's d) of the initialization scheme. Note the different y axes in the plots. **(b)** The distributions of the time constants μ in each temporal scale channel for the leaky integrator models trained on the temporal scaling task. **(c)** Relative variance of the time constants μ for the leaky integrator models as training for the temporal scaling task progresses, averaged across all channels.

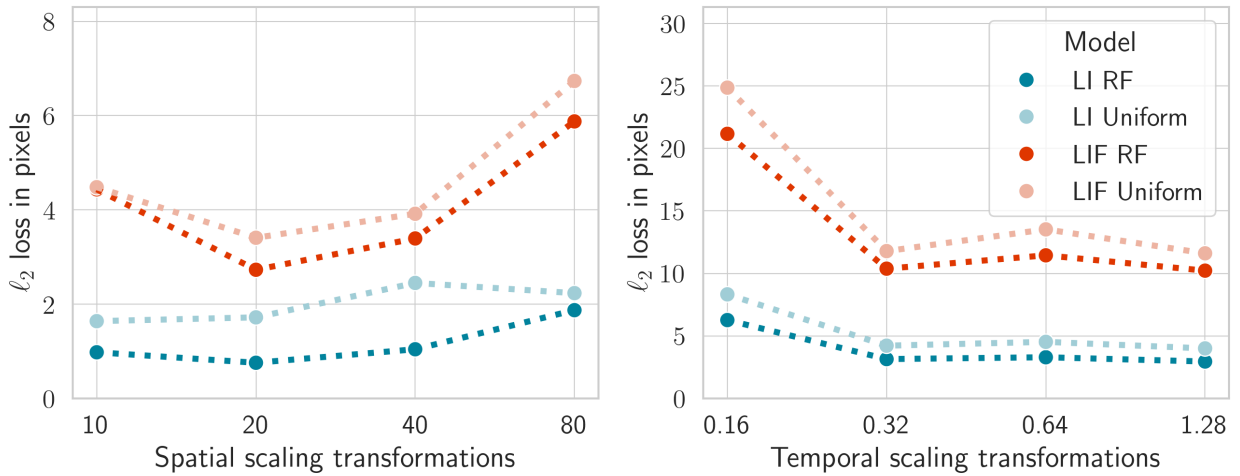


Figure 5: The performance of the trained LI and LIF models when subject to unseen testing data at different scales. Note the different y-axes.

Generalization across scales

Models that are provably covariant to scaling transformations should robustly represent and generalize to other scales [Jansson and Lindeberg, 2021, Lindeberg, 2022]. To study the generalization across varying spatial and temporal scales, we ask the trained models to infer object positions at individual transformational scales.

Figure 5 shows the results for spatial and temporal scaling transformations for the leaky integrate and leaky integrate-and-fire models. The models initialized with spatio-temporal receptive fields are slightly more flat and, therefore, less sensitive to transformations in the data. The spatial models perform relatively worse at the largest scale, which can be explained by the fact that objects that are 80 pixels in diameter are difficult for small convolutional models to capture because they do not fit in any single kernel. Conversely, the temporal models struggle at small velocities. This can be attributed to the fact that the data is extremely sparse when the velocity is low, since the slow rate of movement does not trigger any pixel changes, as described in Section 4 and shown in Figure 8.

Both settings—the large spatial scale and the slow temporal velocities—are detrimental to the leaky integrate-and-fire model because they rely on non-zero inputs to cross the firing threshold. Without enough activity, it will never output any spikes which makes the training even harder. The relatively worse performance compared to the leaky integrator model can additionally be explained by the complicated gradient landscape, introduced by the surrogate gradients.

Relation to batch normalization

It is worth mentioning that receptive fields have a normalizing effect, since they follow scale-normalized derivatives, as described in Section 2 [Lindeberg, 2022]. In deep learning, batch normalization is a popular method to normalize input signals and correct for distributional shifts during learning [Ioffe and Szegedy, 2015]. To study the effect of batch normalization, we experiment with an added layer of batch normalization before each temporal activation layer in the model, available in the Supplementary Material, Section F. As expected, batch normalization removes part of the effect of the initialization. Additionally, since the input is constantly normalized and provide constant non-zero inputs (and, therefore, gradients), the spiking model performs better.

3 Discussion

We presented a theoretically well-founded model for covariant spatio-temporal receptive fields under geometric image transformations and temporally scaled signals, involving leaky integrator and leaky integrate-and-fire neuron models over time. We hypothesized that the initialization of spiking event-driven deep networks with priors from idealized receptive fields improves the training process. Our hypothesis was tested in a neural network on a coordinate regression event-based vision task. The experiments confirmed our theoretical prediction in that correctly initialized spatio-temporal fields significantly improve the performance of event-based networks.

We set out to study principled methods of computation in neuromorphic systems and argue that our findings carry three important implications. Firstly, we conceptually extended the scale-space framework to biologically-inspired and spiking primitives, which provides an exciting direction for principled computation in neuromorphic systems. This establishes a direct link to the large literature around scale-space and conventional computer vision in the context of neuromorphic computing, such as covariant geometric deep learning, which have been successful in computer vision [Cohen and M. Welling, 2016, Bekkers, 2020], polynomial basis expansions for memory representations, known as state space models [Voelker et al., 2019, Gu et al., 2020], and reinforcement learning [Howard et al., 2023]. Additionally, scale-space representations have been related to computation in biological vision systems and the primary visual cortex [Lindeberg, 2021]. The covariance properties in event-based computation align well with experimental findings around time-invariant neural processing [Gütig and Sompolinsky, 2009, Jacques et al., 2022], episodic memory “spectra” [Bright et al., 2020], intrinsic coding of time scales in neural computation [Goel and Buonomano, 2014, Lindeberg, 2023b], and heterogeneous distributions of time constants in spiking networks [Perez-Nieves et al., 2021]. As a second implication, we uncover and exploit powerful intrinsic computational functions of neural circuits. Since the network architecture builds on biologically-inspired primitives and operates without temporal averaging and with asynchronous signals, it is an ideal candidate for implementation in neuromorphic and biophysical systems, possibly via the Neuromorphic Intermediate Representation [Pedersen et al., 2024a]. Third, the immediate practical value of our approach relates to event-based vision tasks and signal processing in real-time settings, in particular when processing data at the edge where resources are scarce and necessarily time-causal. Competing with the performance of ANNs in event-based vision tasks is a crucial step towards the serious use of neuromorphic systems for real-world applications.

This work provided an ideal setting with provable mathematical results that was subsequently demonstrated in a single network for carefully chosen covariance properties. As such, the size of the example network and the limited

$$\begin{array}{ccc}
L(x, t; \Sigma, \tau, v) & \xrightarrow{x' = A(x+ut)} & L'(x', t'; \Sigma', \tau', v') \\
\uparrow & \Sigma' = A \Sigma A^T & \uparrow \\
\star T(x, t; \Sigma, \tau, v) & \tau' = S_t^2 \tau & \star T(x', t'; \Sigma', \tau', v') \\
& v' = (A v + u) / S_t & \\
f(x, t) & \xrightarrow{x' = A(x+ut) \atop t' = S_t t} & f'(x', t')
\end{array}$$

Figure 6: Commutative diagram for convolutions with the spatio-temporal kernel $T(x, t; \Sigma, \tau, v)$ according to Equation (8), which obeys joint covariance under compositions of spatial affine transformations, Galilean transformations, and temporal scaling transformations. The commutative property implies that the order of transformations and spatio-temporal kernel applications is interchangeable.

exploration of hyperparameters restrains the generalization of the method to other networks and tasks without further studies. The theoretical framework operates in the continuous domain, and some assumptions about the distribution and discretization of the spatio-temporal receptive fields may impact model performance. While we argue that the demonstrations here provide a promising step for event-based vision tasks, the findings calls for further experiments to understand how the theoretical guarantees relate to other settings, including different hyperparameters, alternative geometries, and real-life datasets.

Since we base our theoretical findings on the spike-response model, which is powerful enough to describe numerous other neuron models, an interesting avenue for future work is to explore the generalization of our approach to other neuron models, such as the Hodgkin-Huxley model [Hodgkin and Huxley, 1952], the Izhikevich model [Izhikevich, 2003], or the Fitzhugh-Nagumo model [Sherwood, 2013].

The main goal of this work was to establish a theoretical framework for spatio-temporal receptive fields that links computer vision and biologically-inspired computational vision processing. Theory tells us that systems endowed with spatio-temporal receptive fields similar to the ones presented in this paper provide more compact and efficient networks. Our findings show that the initialization of spiking event-driven deep networks with priors from idealized receptive fields improves the training process. While more work is needed to establish the generalization of the approach, we believe that our findings are a step towards more principled computation for vision processing in neuromorphic systems.

4 Methods

Covariance properties of spatio-temporal receptive fields

Consider a composition of the spatio-temporal image transformations defined in Section 2 of the form

$$x' = A(x + ut), \quad (6)$$

$$t' = S_t t, \quad (7)$$

for two video sequences f' and f that are related according to $f'(x', t') = f(x, t)$. Further, define the spatio-temporal scale-space representations L' and L of f' and f , respectively, by convolution of f and f' with the spatio-temporal smoothing kernels according to [Lindeberg, 2016]

$$T(x, t; \Sigma, \tau, v) = g(x - vt; \Sigma) h(t; \tau), \quad (8)$$

where Σ is a spatial covariance matrix that determines the spatial shape of the spatial Gaussian kernel $g(x : \Sigma)$, v denotes an image velocity that specifies the velocity-sensitivity properties of the spatio-temporal receptive fields over joint space-time, and τ denotes the temporal scale of a scale-covariant temporal window function $h(t; \tau)$.

Then, these spatio-temporal image representations over the two spatio-temporal image domains are related according to

$$L'(x', t'; \Sigma', \tau', v') = L(x, t; \Sigma, \tau, v), \quad (9)$$

provided that the parameters (Σ, τ, v) and (Σ', τ', v') of the receptive fields in the two domains, respectively, are related according to

$$\Sigma' = A \Sigma A^T, \quad (10)$$

$$\tau' = S_t^2 \tau, \quad (11)$$

$$v' = (A v + u) / S_t. \quad (12)$$

This result can be proved by composing the individual image transformations in cascade, as treated in Lindeberg [Lindeberg, 2023a]. Figure 6 illustrates the commutative property of the transformations and the capturing mechanism: if an image is transformed (horizontal arrows) and then captured by a scale-space representation (vertical arrows), the result is the same as if we first capture the image and then transform it.

Relationship under geometric image transformations

Lindeberg and Gårding [Lindeberg and Gårding, 1997] established a relationship between two scale-space representations under linear affine transformations [Lindeberg, 2013]. Concretely, if two spatial images $f(x)$ and $f'(x')$ are related according to $x' = A x$, and provided that the two associated covariance matrices Σ and Σ' are coupled according to [Lindeberg and Gårding, 1997, Eq. (16)],

$$\Sigma' = A \Sigma A^T \quad (13)$$

then two spatially smoothed scale-space representations, L and L' , are related according to,

$$L(x; s, \Sigma) = L'(x; s, \Sigma') \quad (14)$$

where s parameterizes scale. When scaling from s to s' by a spatial scaling factor of S_x , we can relate the two scales by $s' = S_x^2 s$ in the following scale-space representations [Lindeberg, 2023a, Eqs. (35) & (36)]

$$L(x; s, \Sigma) = L'(x; s', \Sigma) \quad (15)$$

We exploit these relationships to initialize our spatial and temporal receptive fields by sampling across the parameter space for the spatial affine and temporal scaling operations.

For the spatial transformations, we sample the space of covariance matrices for Gaussian kernels parameterized by their orientation, scale, and skew up to their second derivative. For computing directional derivatives from the images smoothed by affine Gaussian kernels, we apply compact directional derivative masks to the spatially smoothed image data, according to Section 5 in [Lindeberg, 2024], which constitutes a computationally efficient way of computing multiple affine-Gaussian-smoothed directional derivatives for the same input data. Examples of spatial Gaussian derivative kernels and their directional derivatives of different orders are shown in Figure 3 (a). Combined with the convolutional operator, this guarantees covariance under natural image transformations according to Equation (14) in [Lindeberg, 2023a].

To handle temporal scaling transformations, we choose time constants according to a geometric series, which effectively models logarithmically distributed memories of the past [Lindeberg, 2023b, Eqs. (18)-(20)]

$$\tau_k = c^{2(k-K)} \tau_{\max}, \quad (16)$$

where c is a distribution parameter that we set to $\sqrt{2}$, K is the number of scales, and τ_{\max} is the maximum temporal scale. Further details are available in Supplementary Material Section B.1.

This logarithmic space of scales guarantees *time-causal* self-similar treatment over temporal image scaling operations [Lindeberg and Fagerström, 1996, Lindeberg, 2023a].

Temporal scale covariance for leaky integrator models

The generalized Gaussian derivative model for receptive fields [Lindeberg, 2016, Lindeberg, 2021] defines a spatio-temporal scale-space representation

$$L(x, y; \Sigma, \tau, v) = \int_{\xi \in \mathbb{R}^2} \int_{u \in \mathbb{R}} T(\xi, u; \Sigma, \tau, v) f(\xi, u) d\xi du \quad (17)$$

over joint space-time ($x \in \mathbb{R}^2, t \in \mathbb{R}$) by convolving any video sequence $f(x, t)$ with a spatio-temporal convolution kernel of the form (9)

Previous Gaussian derivative models have exclusively been based on linear receptive fields, as detailed in Section 4 and in the Supplementary Materials Section B. Gaussian kernels are symmetric around the origin and therefore impractical to use as temporal kernels in real-time situations, because they violate the principle of temporal causality. Lindeberg and Fagerström [Lindeberg and Fagerström, 1996] showed that one-sided, truncated exponential temporal scale-space kernels constitute a canonical class of temporal smoothing kernels, in that they are the only time-causal kernels that guarantee non-creation of new structure, in terms of either local extrema or zero-crossings, from finer to coarser levels of scale:

$$h_{exp}(t, \mu) = \begin{cases} \frac{1}{\mu} e^{-t/\mu} & t > 0, \\ 0 & t \leq 0, \end{cases} \quad (18)$$

where the time constant μ represents the temporal scale parameter corresponding to $\tau = \mu^2$ in (8).

Coupling K such temporal filters in parallel, for $k \in [1, K]$, yields a temporal multi-channel representation in the limit when $K \rightarrow \infty$:

$$h_{composed}(\cdot; \tau_k) = h_{exp}(\cdot; \mu_k). \quad (19)$$

A specific temporal scale-space channel representation L for some signal f [Lindeberg and Fagerström, 1996, Eq. (14)] can be written as

$$L(t; \mu) = \int_{u=0}^{\infty} f(t-u) h_{exp}(\cdot; \mu) du. \quad (20)$$

Turning to the domain of neuron models, a first-order integrator with a leak has the following integral representations for a given time t , time constant μ and some time-dependent input I [Gerstner et al., 2014, Eq. (1.11)]:

$$u(t; \mu) = \int_0^{\infty} \frac{1}{\mu} e^{-\xi/\mu} I(t-\xi) d\xi. \quad (21)$$

This precisely corresponds to the truncated exponential kernel in (18). Inserting into (20), we apply the temporal scaling operation $t' = S_t t$ for a temporal scaling factor $S_t > 0$ to the temporal input signals $f'(t') = f(t)$:

$$\begin{aligned} L(t'; \mu') &= \int_{u'=0}^{\infty} f'(t'-u') \frac{1}{\mu'} e^{-t'/\mu'} du' \\ &\stackrel{(1)}{=} \int_{u=0}^{\infty} f'(S_t(t-u)) \frac{1}{S_t \mu} e^{-S_t t/S_t \mu} S_t du \\ &= \int_{u=0}^{\infty} f(t-u) \frac{1}{\mu} e^{-t/\mu} du \\ &= L(t; \mu), \end{aligned} \quad (22)$$

where the step (1) sets $u' = S_t u$, $du' = S_t du$, and $\mu' = S_t \mu$. This establishes temporal scale covariance for a single temporal filter $T(t; \tau) = h_{exp}(t; \mu)$, while a set of temporal filters will be scale-covariant across multiple scales, provided the scales are logarithmically distributed [Lindeberg, 2023a, Section 3.2].

Temporal scale covariance for leaky integrate-and-fire models

Continuing with the thresholded model of the first-order leaky integrator equation, we turn to the Spike Response Model defined in Section ‘‘Spike response model’’ below [Gerstner et al., 2014]. This model generalizes to numerous neuron models, but we will restrict ourselves to the leaky integrate-and-fire equations, which can be viewed as the composition of three filters: a membrane filter κ , a threshold filter H , and a membrane reset filter η' . In the case of the leaky integrate-and-fire model, we know that the resetting mechanism, as determined by η' , depends entirely on the spikes, and we can decouple it from the spike function Γ . If we further assume that the membrane reset follows a linear decay, governed by a time constant μ_r , of the form described in Equation (30) in the Methods section, we arrive at the following formula for the leaky integrate-and-fire model:

$$z(t) = -\theta_{thr} e^{-(t-t_f)/\mu_r} + \int_0^{\infty} \kappa(s) I(t-s) ds. \quad (23)$$

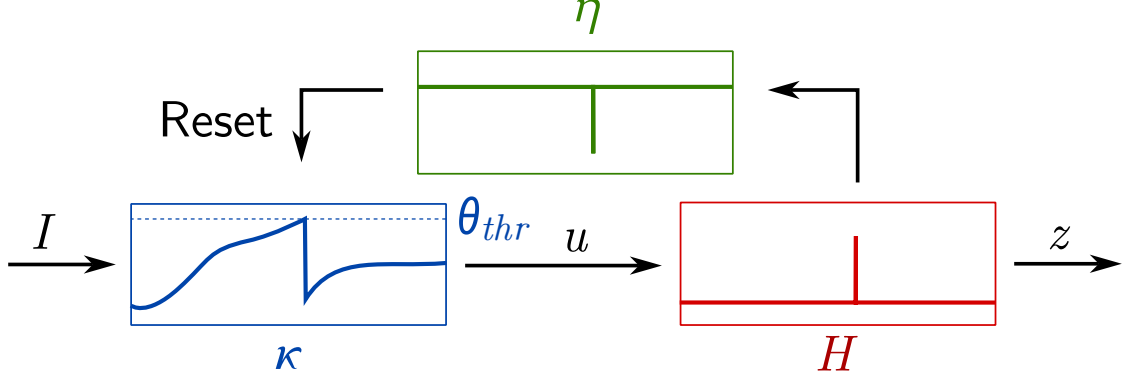


Figure 7: The spike response model recasts the leaky integrate-and-fire model as a composition of three filters: a membrane filter in blue (κ), a threshold filter in red (H), and a reset filter in green (η). The graphs inside the filters depict their respective outputs over time using the kernels in (28), given some input signal, I .

Considering a temporal scaling transformation $t' = S_t t$ and $t'_f = S_t t_f$ for the temporal signals $f'(t') = f(t)$ in the concrete case of $\kappa = h_{exp}$, we follow the steps in Equation (22):

$$\begin{aligned}
 L(t'; \mu', \mu_r') &= -\theta_{thr} e^{-(t'-t'_f)/\mu_r'} + \int_{z'=0}^{\infty} f'(t' - z') \frac{1}{\mu'} e^{-t'/\mu'} dz' \\
 &\stackrel{(22)}{=} -\theta_{thr} e^{-S_t(t-t_f)/S_t \mu_r'} + \int_{z=0}^{\infty} f'(S_t(t - z)) \frac{1}{S_t \mu} e^{-S_t t/S_t \mu} S_t dz \\
 &= -\theta_{thr} e^{-(t-t_f)/\mu_r} + \int_{z=0}^{\infty} f(t - z) \frac{1}{\mu} e^{-t/\mu} dz \\
 &= L(t; \mu, \mu_r).
 \end{aligned} \tag{24}$$

This shows that a single leaky integrate-and-fire filter z is scale covariant over time, and can be extended to a spectrum of temporal scales as above. Combined with the spatial affine covariance as well as Galilean covariance from Equation (9), this finding establishes spatio-temporal covariance to spatial affine transformations, Galilean transformations and temporal scaling transformations in the image plane for leaky integrators and leaky integrate-and-fire neurons.

Spiking neuron models

We use the leaky integrate-and-fire formalization from Lapicque [Blair, 1932, Abbott, 1999], stating that a neuron voltage potential u evolves over time, according to its time constant, μ , and some input current I

$$\mu \dot{u} = -u + I \tag{25}$$

with the Heaviside threshold function parameterized by $\theta_{threshold}$

$$z(t) = \begin{cases} 1 & u \geq \theta_{threshold} \\ 0 & u < \theta_{threshold} \end{cases} \tag{26}$$

and a jump condition for the membrane potential, which resets to θ_{reset} when the threshold is crossed

$$u(t) = \begin{cases} \theta_{reset} & z(t) = 1 \\ u(t) & z(t) < 1 \end{cases} \tag{27}$$

The *firing* part of the leaky integrate-and-fire model implies that neurons are coupled solely at discrete events, known as spikes.

Spike response model

The Spike Response Model describes neuronal dynamics as a compositions of filters [Gerstner et al., 2014], a membrane filter (κ), a threshold filter (H), and a membrane reset filter (η) shown in Figure 7. Consider a reset filter (η') applied to a spike generating function (Γ) and a subthreshold integration term (κ) given some input current (I):

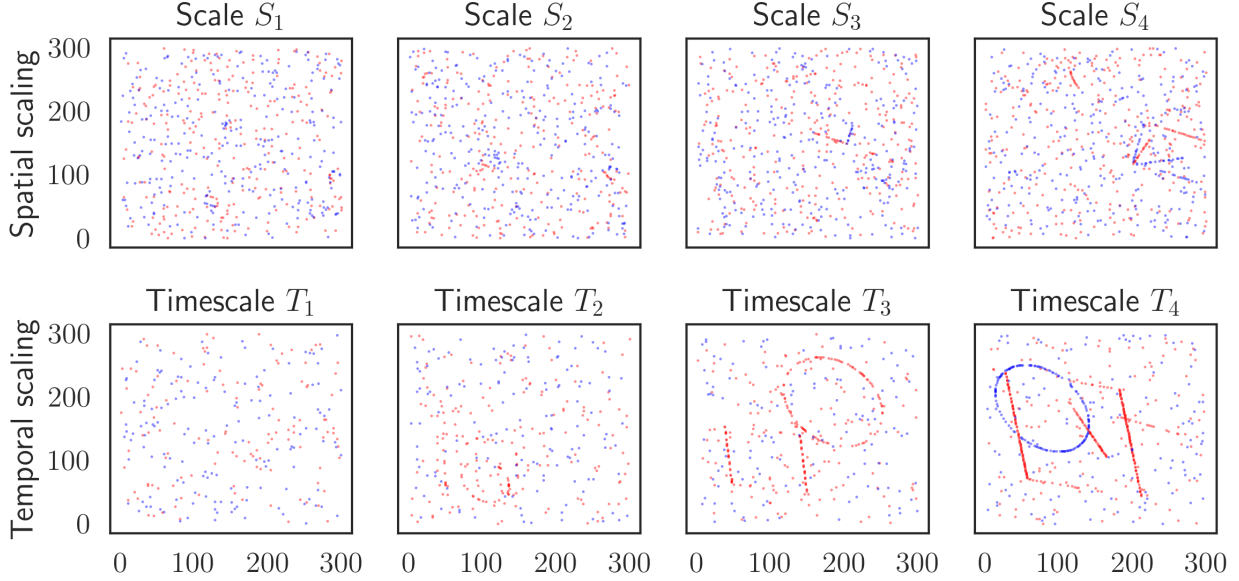


Figure 8: Image snapshots from the two synthetic datasets used in this work. The top row shows the four different spatial scaling, corresponding to shapes of 10, 20, 40, and 80 pixels. The bottom row shows the four different temporal velocities, corresponding to a change of 0.16, 0.32, 0.64, and 1.28 pixels per timestep. Both datasets are extremely sparse, with the shapes barely visible in the images. At larger temporal velocities, the shapes become more discernible.

$$u(t) = \int_0^\infty \eta'(s) \Gamma(t-s) + \kappa(s) I(t-s) ds \quad (28)$$

The reset filter, η' , is the resetting mechanism of the neuron, that is, the function dominating the subthreshold behavior immediately after a spike. We now recast the reset mechanism as a function of time (t), where t_f denotes the time of the previous spike

$$u(t) = \eta(t - t_f) + \int_0^\infty \kappa(s) I(t-s) ds \quad (29)$$

Following [Gerstner et al., 2014, Eq. (6.33)] we define η more concretely as a linearized reset mechanism for the LIF model

$$\eta(t - t_f; \mu_r) = -\theta_{thr} e^{-(t-t_f)/\mu_r} \quad (30)$$

which describes the “after-spike effect”, decaying at a rate determined by μ_r . Immediately following a spike, $e^0 = 1$ and the kernel corresponds to the *negative* value of θ_{thr} at the time of the spike, effectively resetting the membrane potential by θ_{thr} . In the LIF model, the reset is instantaneous, which we observe when $\mu_r \rightarrow 0$. Figure 7 shows the set of filters correspond to the subthreshold mechanism in Equation (21) (which we know to be scale covariant from Equations (22)), the Heaviside threshold, and the reset mechanism in Equation (30). We arrive at the following expression for the subthreshold voltage dynamics for the spike response model

$$z(t) = -\theta_{thr} e^{-(t-t_f)/\mu_r} + \int_0^\infty \kappa(s) I(t-s) ds \quad (31)$$

where κ can be replaced by h_{exp} for the leaky integrate-and-fire model.

Dataset

We simulate an event-based dataset consisting of sparse shape contours, as shown in Figure 8, based on [Pedersen et al., 2024b]. Events are generated by applying some transformation A to the shapes and subtracting two subsequent frames. We then integrate those differences over time until for each pixel, until reaching a certain threshold and emitting events of either positive or negative polarity. This approximates the dynamics of event cameras, which

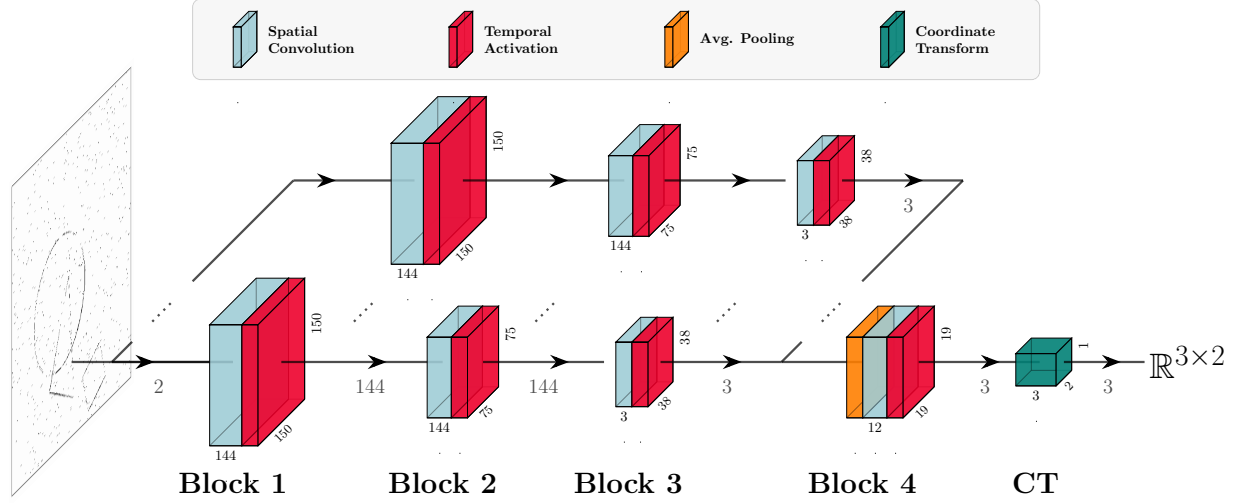


Figure 9: The network architecture. The first three convolutional blocks are parallelized into four different temporal scale channels that are sensitive to different temporal scales. Block 4 merges all the channels and produces three object-specific output channels that are transformation into coordinates in \mathbb{R}^2 in the Coordinate Transformation (CT) block. Those coordinates are compared to the labelled position of the sparse event-based shapes in the dataset. When initializing models according to theory, the two first blocks are configured as described in Section “Parameter initialization” below. Parameters in the remaining two blocks are uniformly initialized except the temporal activation time constant in Block 3, which is fixed to the fastest time constant.

emit discrete events when the intensity changes by a certain threshold [Lichtsteiner et al., 2008]. To obtain sub-pixel accuracy we perform all transformations in a high-resolution space of 2400×2400 pixels, which is downsampled bilinearly to the dataset resolution of 300×300 .

We use three simple geometries, a triangle, a square, and a circle, that are translated with random motion sampled from the same uniform distribution. The shapes are positioned randomly in the image and oriented by a random, fixed, angle. Two datasets are studied: one with varying spatial scales and one with varying temporal velocities. In the spatial scale dataset, the starting scale of the shape is logarithmically distributed from 10 to 80 pixels. In the temporal velocity dataset, the shapes scale logarithmically from ± 0.16 to ± 1.28 pixels. The velocities are normalized to the subsampled pixel space such that, for translational velocity for example, a velocity of one in the x -axis corresponds to the shape moving one pixel in the x -axis per timestep. The velocity parameterizes the sparsity of the temporal scaling dataset, as seen in the bottom row in Figure 8 panel, where the shape contours in the left panels are barely visible compared to the faster-moving objects in the right panels. To simulate noise, we add 5 % Bernoulli-distributed background noise.

The data is extremely sparse, even with high velocities. A temporal velocity of 0.16 provides around 3% activations while a scale of 1.28 provides around 2% activations, including noise. Furthermore, random guessing yields an average ℓ^2 error of 152 pixels when both points are drawn uniformly from a 300×300 cube [OEIS Foundation Inc., 2024]. If one of the points is fixed to the center of the cube, the error averages to 76 pixels.

Model architecture and training

Figure 9 shows our network architecture, which combines a distribution of spatial receptive fields expanded over 4 parallel spatio-temporal scale channels into a single convolutional block. A scale channel is defined as a sequence of spatio-temporal receptive fields represented as convolutional blocks, where each block consists of a spatial convolution, and an activation function (a temporal and causal convolution).

The model architecture is fixed in all the experiments, but four different activation functions are studied in the scale channel blocks: a leaky integrator (LI), a leaky integrate-and-fire model (LIF), a ReLU, and a ReLU with additional historical information. The first two such functions are the leaky integrator, coupled with a rectified linear unit (ReLU) to induce a (spatial) nonlinearity, and the leaky integrate-and-fire models. To provide baseline comparisons to stateless models, we additionally construct a stateless Single Frame (SF) model, that uses ReLU activations instead of the temporal kernels, and a Multiple Frame (MF) model, that operates on eight consecutive frames instead of one. We

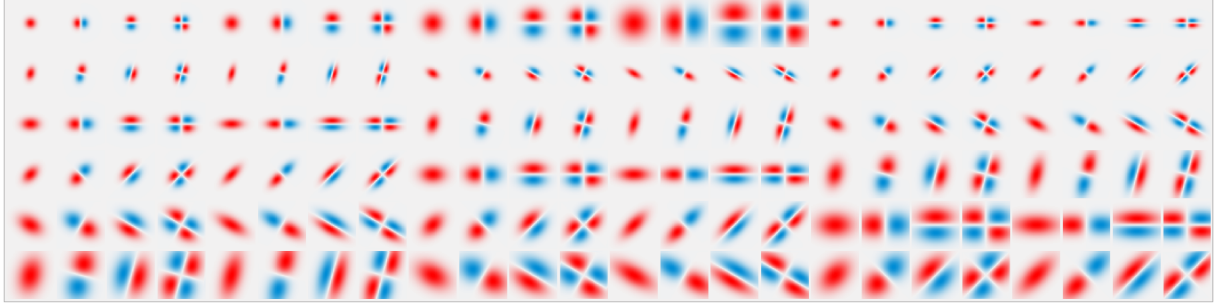


Figure 10: Distribution of 144 spatial receptive fields for the convolutional blocks in the model at a high resolution. The kernels in the deep network are initialized from this distribution, obtained by sampling over the space of spatial transformations and their derivatives. For the discrete implementation model, these continuous kernels are downsampled to 9×9 pixels.

chose eight frames for the frame-based model since it compares to an exponentially decaying leaky integrator with $\mu = 2$ which, after 8 timesteps, only retains about 2% of the original signal, specifically $\exp(-\frac{8}{2}) = 0.0183\%$.

To convert the latent activation space from the fourth block into 2-dimensional coordinates on which we can regress, we apply a differentiable coordinate transformation layer introduced in [Pedersen et al., 2023], that finds the spatial average in two dimensions for each of the three shapes, as shown in Figure 9. Note that the coordinate transform uses leaky integrator neurons for both the spiking and non-spiking model architectures.

Training

We train the models using backpropagation through time on datasets consisting of movies with 50 frames of 1 ms duration, with 20 % of the dataset held for model validation. The full sets of parameters, along with steps to reproduce the experiments, are available in the Supplementary Material and online at <https://github.com/jegp/nrf>.

Parameter initialization

The spatial and temporal receptive fields, that constitute the spatio-temporal blocks above, are initialized by sampling over the space of all possible geometric image transformations according to Equations (10), (11), and (12). Figure 1 illustrates a sample of 4×4 different spatial scales $\sigma \in \{1, 2, 4, 8\}$ and temporal scales $\mu \in \{1, 2, 4, 8\}$, whereas Figure 2 is restricted to three temporal scales ($\mu \in \{8, 4, 2\}$).

The geometric image transformations are modeled via spatial affine operations A , image velocities v , and constant shifts u , where the covariance matrices Σ of the affine Gaussian kernels are influenced by the affine transformations A according to Equation (10). We parameterize each receptive field according to the orientation, scale, and skew of the covariance matrix, as well as the n :th-order derivative of the receptive field, as described in Equation (5). The temporal transformation is of the form (11) and is controlled by the time constant τ , determined from the time constants μ in the first order integrators (21) and (23) according to $\tau = \mu^2$.

Ideally, we wish to measure the continuous change for all the parameters above, but we restrict the models to 144 spatial convolutional kernels per block and 4 temporal scales. The spatial kernels are linearly sampled over 4 orientations, 4 spatial scales, 3 skewness values, and derivative orders of zeroth, first orders (δ_x, δ_y), and one second order derivative (δ_{xy}) shown in Figure 10. We sample the time constants according to the geometric series in Equation (16) with $K = 4$ scales and the distribution parameter $c = \sqrt{2}$. We uniformly initialize the spatial convolutional kernels in the third and fourth blocks, to allow higher-order features to form that may be data-dependent and not captured by the theory.

Initialization effect size

To quantify the effect of the initialization, we measure the size of the effect on the model’s performance, described as the difference in the mean loss values ℓ between the mean of the initialized ℓ_{init} and the mean of the uniformly initialized ℓ_{uniform} models. Since we are working with multiple evaluations of the same model, we correct for the

spread of the distributions using the “pooled standard deviation” σ_{pool} :

$$\text{Effect size} = \frac{\ell_{\text{init}} - \ell_{\text{uniform}}}{\sigma_{\text{pool}}}. \quad (32)$$

The pooled standard deviation is calculated following [Cohen, 1969], where n_i is the number of samples in the i :th group,

$$\sigma_{\text{pool}} = \sqrt{\frac{(n_1 - 1)\sigma_1^2 + (n_2 - 2)\sigma_2^2}{n_1 + n_2 - 2}}, \quad (33)$$

and σ^2 is the variance of the samples defined by

$$\sigma^2 = \frac{\sum_{i=1}^N (n_i - 1)\sigma_i^2}{\sum_{i=1}^N (n_i - 1)}, \quad (34)$$

The standardized effect size indicates the number of standard deviations the mean of the initialized models is from the mean of the uniformly initialized models. More than two standard deviations implies a large and significant effect.

5 Acknowledgements

The authors gratefully acknowledge support from the EC Horizon 2020 Framework Programme under Grant Agreements 785907 and 945539 (HBP), the Swedish Research Council under contracts 2022-02969 and 2022-06725, and the Danish National Research Foundation grant number P1.

6 Reproducibility and data availability

All material, code, and data required to reproduce the results in this paper can be found at <https://github.com/jegp/nrf>. All simulations, neuron models, and the spatio-temporal receptive fields rely on the Norse library [Pehle and Pedersen, 2021]. The implementation of affine directional derivatives is based on the affscsp module in the pyscsp package available from <https://github.com/tonylindeberg/pyscsp> and some parts of the temporal smoothing operations are based on the pytempscsp package available from <https://github.com/tonylindeberg/pytempscsp>.

References

- [Abbott, 1999] Abbott, L. F. (1999). Lapicque’s introduction of the integrate-and-fire model neuron (1907). *Brain Research Bulletin*, 50(5):303–304.
- [Aimone and Parekh, 2023] Aimone, J. B. and Parekh, O. (2023). The brain’s unique take on algorithms. *Nature Communications*, 14(11):4910.
- [Arnold et al., 2023] Arnold, E., Böcherer, G., Strasser, F., Müller, E., Spilger, P., Billaudelle, S., Weis, J., Schemmel, J., Calabro, S., and Kuschnnerov, M. (2023). Spiking neural network nonlinear demapping on neuromorphic hardware for IM/DD optical communication. *Journal of Lightwave Technology*, 41:3424–3431.
- [Barranco et al., 2015] Barranco, F., Teo, C. L., Fermüller, C., and Aloimonos, Y. (2015). Contour detection and characterization for asynchronous event sensors. In *2015 IEEE International Conference on Computer Vision (ICCV)*, pages 486–494.
- [Bekkers, 2020] Bekkers, E. J. (2020). B-spline CNNs on Lie groups. *International Conference on Learning Representations (ICLR 2020)*.
- [Blair, 1932] Blair, H. A. (1932). On the intensity-time relations for stimulation by electric currents. i. *Journal of General Physiology*, 15(6):709–729.
- [Bretzner and Lindeberg, 1998] Bretzner, L. and Lindeberg, T. (1998). Feature tracking with automatic selection of spatial scales. *Computer Vision and Image Understanding*, 71(3):385–392.
- [Bright et al., 2020] Bright, I., Meister, M. L. R., Cruzado, N. A., Tiganj, Z., Buffalo, E. A., and Howard, M. W. (2020). A temporal record of the past with a spectrum of time constants in the monkey entorhinal cortex. *Proceedings of the National Academy of Sciences*, 117(33):20274–20283.

[Cohen, 1969] Cohen, J. (1969). Statistical power analysis for the behavioral sciences. *The SAGE Encyclopedia of Research Design*.

[Cohen and M. Welling, 2016] Cohen, T. and M. Welling, M. (2016). Group equivariant convolutional networks. In *International Conference on Machine Learning (ICML 2016)*, pages 2990–2999.

[Delbrück and Lang, 2013] Delbrück, T. and Lang, M. (2013). Robotic goalie with 3 ms reaction time at 4% CPU load using event-based dynamic vision sensor. *Frontiers in Neuroscience*, 7.

[Eliasmith and Anderson, 2004] Eliasmith, E. and Anderson, C. H. (2004). Neural engineering: Computation, representation, and dynamics in neurobiological systems. *IEEE Transactions on Neural Networks*, 15(2):528–529.

[Eshraghian et al., 2023] Eshraghian, J. K., Ward, M., Neftci, E. O., Wang, X., Lenz, G., Dwivedi, G., Bennamoun, M., Jeong, D. S., and Lu, W. D. (2023). Training spiking neural networks using lessons from deep learning. *Proceedings of the IEEE*, 111(9):1016–1054.

[Evans et al., 2022] Evans, B. D., Malhotra, G., and Bowers, J. S. (2022). Biological convolutions improve DNN robustness to noise and generalisation. *Neural Networks*, 148:96–110.

[Folowosele et al., 2011] Folowosele, F., Vogelstein, R. J., and Etienne-Cummings, R. (2011). Towards a cortical prosthesis: Implementing a spike-based hmax model of visual object recognition in silico. *IEEE Journal on Emerging and Selected Topics in Circuits and Systems*, 1(4):516–525.

[Fukushima et al., 1970] Fukushima, K., Yamaguchi, Y., Yasuda, M., and Nagata, S. (1970). An electronic model of the retina. *Proceedings of the IEEE*, 58(12):1950–1951.

[Gallego et al., 2022] Gallego, G., Delbrück, T., Orchard, G., Bartolozzi, C., Taba, B., Censi, A., Leutenegger, S., Davison, A. J., Conradt, J., Daniilidis, K., and Scaramuzza, D. (2022). Event-based vision: A survey. *IEEE Transactions on Pattern Analysis and Machine Intelligence*, 44(1):154–180.

[Gerstner et al., 2014] Gerstner, W., Kistler, W. M., Naud, R., and Paninski, L. (2014). *Neuronal Dynamics: From Single Neurons to Networks and Models of Cognition*. Cambridge University Press, Cambridge.

[Ghosh et al., 2014] Ghosh, R., Mishra, A., Orchard, G., and Thakor, N. V. (2014). Real-time object recognition and orientation estimation using an event-based camera and CNN. In *2014 IEEE Biomedical Circuits and Systems Conference (BioCAS) Proceedings*, pages 544–547.

[Goel and Buonomano, 2014] Goel, A. and Buonomano, D. V. (2014). Timing as an intrinsic property of neural networks: evidence from in vivo and in vitro experiments. *Philosophical Transactions of the Royal Society B: Biological Sciences*, 369(1637):20120460.

[Gu et al., 2020] Gu, A., Dao, T., Ermon, S., Rudra, A., and Re, C. (2020). HiPPO: Recurrent memory with optimal polynomial projections. (arXiv:2008.07669). arXiv:2008.07669 [cs, stat].

[Gütig and Sompolinsky, 2009] Gütig, R. and Sompolinsky, H. (2009). Time-warp-invariant neuronal processing. *PLOS Biology*, 7(7):e1000141.

[Hodgkin and Huxley, 1952] Hodgkin, A. L. and Huxley, A. F. (1952). Currents carried by sodium and potassium ions through the membrane of the giant axon of loligo. *The Journal of Physiology*, 116(4):449–472.

[Howard et al., 2023] Howard, M. W., Esfahani, Z. G., Le, B., and Sederberg, P. B. (2023). Foundations of a temporal RL. (arXiv:2302.10163). arXiv:2302.10163 [q-bio].

[Hubel and Wiesel, 1962] Hubel, D. H. and Wiesel, T. N. (1962). Receptive fields, binocular interaction and functional architecture in the cat’s visual cortex. *The Journal of Physiology*, 160(1):106–154.2.

[Ioffe and Szegedy, 2015] Ioffe, S. and Szegedy, C. (2015). Batch normalization: Accelerating deep network training by reducing internal covariate shift. In *Proceedings of the 32nd International Conference on Machine Learning*, page 448–456. PMLR.

[Izhikevich, 2003] Izhikevich, E. (2003). Simple model of spiking neurons. *IEEE Transactions on Neural Networks*, 14(6):1569–1572.

[Jacobsen et al., 2016] Jacobsen, J.-J., van Gemert, J., Lou, Z., and Smeulders, A. W. M. (2016). Structured receptive fields in CNNs. In *Proc. Computer Vision and Pattern Recognition (CVPR 2016)*, pages 2610–2619.

[Jacques et al., 2022] Jacques, B. G., Tiganj, Z., Sarkar, A., Howard, M., and Sederberg, P. (2022). A deep convolutional neural network that is invariant to time rescaling. In *Proceedings of the 39th International Conference on Machine Learning*, page 9729–9738. PMLR.

[Jansson and Lindeberg, 2018] Jansson, Y. and Lindeberg, T. (2018). Dynamic texture recognition using time-causal and time-recursive spatio-temporal receptive fields. *Journal of Mathematical Imaging and Vision*, 60(9):1369–1398.

[Jansson and Lindeberg, 2021] Jansson, Y. and Lindeberg, T. (2021). Exploring the ability of CNNs to generalise to previously unseen scales over wide scale ranges. page 1181–1188.

[Kingma and Ba, 2014] Kingma, D. P. and Ba, J. (2014). Adam: A method for stochastic optimization. *CoRR*, abs/1412.6980.

[Koenderink, 1984] Koenderink, J. (1984). The structure of images. *Biological Cybernetics*, 50(5):363–370.

[Koenderink, 1988] Koenderink, J. (1988). Scale-time. *Biological Cybernetics*, 58(3):159–162.

[Koenderink and van Doorn, 1976] Koenderink, J. and van Doorn, A. J. (1976). Geometry of binocular vision and a model for stereopsis. *Biological Cybernetics*, 21(1):29–35.

[Kreutzer et al., 2020] Kreutzer, E., Petrovici, M. A., and Senn, W. (2020). Natural gradient learning for spiking neurons. *Proceedings of the Neuro-inspired Computational Elements Workshop*, pages 1–3. Conference Name: NICE '20: Neuro-inspired Computational Elements Workshop ISBN: 9781450377188 Place: Heidelberg Germany Publisher: ACM.

[Lagorce et al., 2017] Lagorce, X., Orchard, G., Galluppi, F., Shi, B. E., and Benosman, R. B. (2017). HOTS: A hierarchy of event-based time-surfaces for pattern recognition. *IEEE Transactions on Pattern Analysis and Machine Intelligence*, 39(7):1346–1359.

[Lecun et al., 1998] Lecun, Y., Bottou, L., Bengio, Y., and Haffner, P. (1998). Gradient-based learning applied to document recognition. *Proceedings of the IEEE*, 86(11):2278–2324.

[Lettvin et al., 1959] Lettvin, J. Y., Maturana, H. R., McCulloch, W. S., and Pitts, W. H. (1959). What the frog's eye tells the frog's brain. *Proceedings of the IRE*, 47(11):1941–1951.

[Lichtsteiner et al., 2008] Lichtsteiner, P., Posch, C., and Delbrück, T. (2008). A 128x128 120 dB 15 microsecond latency asynchronous temporal contrast vision sensor. *IEEE Journal of Solid-State Circuits*, 43(2):566–576.

[Lindeberg, 1994] Lindeberg, T. (1994). *Scale-Space Theory in Computer Vision*. Springer US, Boston, M.

[Lindeberg, 1998] Lindeberg, T. (1998). Feature detection with automatic scale selection. *International Journal of Computer Vision*, 30(2):77–116.

[Lindeberg, 2013] Lindeberg, T. (2013). A computational theory of visual receptive fields. *Biological Cybernetics*, 107(6):589–635.

[Lindeberg, 2015] Lindeberg, T. (2015). Image matching using generalized scale-space interest points. *Journal of Mathematical Imaging and Vision*, 52(1):3–36.

[Lindeberg, 2016] Lindeberg, T. (2016). Time-causal and time-recursive spatio-temporal receptive fields. *Journal of Mathematical Imaging and Vision*, 55(1):50–88.

[Lindeberg, 2017] Lindeberg, T. (2017). Temporal scale selection in time-causal scale space. *Journal of Mathematical Imaging and Vision*, 58(1):57–101.

[Lindeberg, 2018] Lindeberg, T. (2018). Spatio-temporal scale selection in video data. *Journal of Mathematical Imaging and Vision*, 60(4):525–562.

[Lindeberg, 2021] Lindeberg, T. (2021). Normative theory of visual receptive fields. *Heliyon*, 7(1):e05897.

[Lindeberg, 2022] Lindeberg, T. (2022). Scale-covariant and scale-invariant Gaussian derivative networks. *Journal of Mathematical Imaging and Vision*, 64(3):223–242.

[Lindeberg, 2023a] Lindeberg, T. (2023a). Covariance properties under natural image transformations for the generalized Gaussian derivative model for visual receptive fields. *Frontiers in Computational Neuroscience*, 17:1189949.

[Lindeberg, 2023b] Lindeberg, T. (2023b). A time-causal and time-recursive scale-covariant scale-space representation of temporal signals and past time. *Biological Cybernetics*, 117:21–59.

[Lindeberg, 2024] Lindeberg, T. (2024). Discrete approximations of Gaussian smoothing and Gaussian derivatives. *Journal of Mathematical Imaging and Vision*, 66(5):759–800.

[Lindeberg and Fagerström, 1996] Lindeberg, T. and Fagerström, D. (1996). *Scale-space with causal time direction*, volume 1064 of *Lecture Notes in Computer Science*, pages 229–240. Springer Berlin Heidelberg, Berlin, H.

[Lindeberg and Gårding, 1997] Lindeberg, T. and Gårding, J. (1997). Shape-adapted smoothing in estimation of 3-D shape cues from affine distortions of local 2-D structure. *Image and Vision Computing*, 15:415–434.

[Litzenberger et al., 2006] Litzenberger, M., Posch, C., Bauer, D., Belbachir, A., Schon, P., Kohn, B., and Garn, H. (2006). Embedded vision system for real-time object tracking using an asynchronous transient vision sensor. In *2006 IEEE 12th Digital Signal Processing Workshop & 4th IEEE Signal Processing Education Workshop*, pages 173–178.

[Lowe, 2004] Lowe, D. G. (2004). Distinctive image features from scale-invariant keypoints. *International Journal of Computer Vision*, 60(2):91–110.

[Maass, 1997] Maass, W. (1997). Networks of spiking neurons: The third generation of neural network models. *Neural Networks*, 10(9):1659–1671.

[Mead, 1989] Mead, C. (1989). *Analog VLSI and neural systems*. Reading, Mass. Addison-Wesley.

[Mead, 2023] Mead, C. (2023). Neuromorphic engineering: In memory of Misha Mahowald. *Neural Computation*, 35(3):343–383.

[Mikolajczyk and Schmid, 2004] Mikolajczyk, K. and Schmid, C. (2004). Scale and affine invariant interest point detectors. *International Journal of Computer Vision*, 60(1):63–86.

[Miri et al.,] Miri, A., Bhasin, B. J., Aksay, E. R. F., Tank, D. W., and Goldman, M. S. Oculomotor plant and neural dynamics suggest gaze control requires integration on distributed timescales. 600(16):3837–3863.

[Nagaraj et al., 2023] Nagaraj, M., Liyanagedera, C. M., and Roy, K. (2023). DOTIE - detecting objects through temporal isolation of events using a spiking architecture. In *2023 IEEE International Conference on Robotics and Automation (ICRA)*, pages 4858–4864.

[Neftci et al., 2019] Neftci, E. O., Mostafa, H., and Zenke, F. (2019). Surrogate gradient learning in spiking neural networks: Bringing the power of gradient-based optimization to spiking neural networks. *IEEE Signal Processing Magazine*, 36(6):51–63.

[Ni et al., 2012] Ni, Z., Bolopion, A., Agnus, J., Benosman, R., and Regnier, S. (2012). Asynchronous event-based visual shape tracking for stable haptic feedback in microrobotics. *IEEE Transactions on Robotics*, 28(5):1081–1089.

[OEIS Foundation Inc., 2024] OEIS Foundation Inc. (2024). The On-Line Encyclopedia of Integer Sequences. Published electronically at <http://oeis.org>.

[Orchard et al., 2015] Orchard, G., Meyer, C., Etienne-Cummings, R., Posch, C., Thakor, N., and Benosman, R. (2015). HFIRST: A temporal approach to object recognition. *IEEE Transactions on Pattern Analysis and Machine Intelligence*, 37(10):2028–2040.

[Pedersen et al., 2024a] Pedersen, J. E., Abreu, S., Jobst, M., Lenz, G., Fra, V., Bauer, F. C., Muir, D. R., Zhou, P., Vogginger, B., Heckel, K., Urgese, G., Shankar, S., Stewart, T. C., Sheik, S., and Eshraghian, J. K. (2024a). Neuromorphic intermediate representation: A unified instruction set for interoperable brain-inspired computing. volume 15, page 8122. Nature Publishing Group.

[Pedersen et al., 2024b] Pedersen, J. E., Korakovounis, D., and Conradt, J. (2024b). Gerd: Geometric event response data generation. (arXiv:2412.03259). arXiv:2412.03259 [cs].

[Pedersen et al., 2023] Pedersen, J. E., Singhal, R., and Conradt, J. (2023). Translation and scale invariance for event-based object tracking. In *Proceedings of the 2023 Annual Neuro-Inspired Computational Elements Conference, NICE '23*, pages 79–85, New York, NY, USA. Association for Computing Machinery.

[Pehle and Pedersen, 2021] Pehle, C.-G. and Pedersen, J. E. (2021). Norse - a deep learning library for spiking neural networks.

[Perez-Nieves et al., 2021] Perez-Nieves, N., Leung, V. C. H., Dragotti, P. L., and Goodman, D. F. M. (2021). Neural heterogeneity promotes robust learning. *Nature Communications*, 12(1):5791.

[Porcu et al., 2021] Porcu, E., Furrer, R., and Nychka, D. (2021). 30 years of space-time covariance functions. *WIREs Computational Statistics*, 13(2):e1512.

[Richards et al., 2019] Richards, B. A., Lillicrap, T. P., Beaudoin, P., Bengio, Y., Bogacz, R., Christensen, A., Clopath, C., Costa, R. P., de Berker, A., Ganguli, S., Gillon, C. J., Hafner, D., Kepecs, A., Kriegeskorte, N., Latham, P., Lindsay, G. W., Miller, K. D., Naud, R., Pack, C. C., Poirazi, P., Roelfsema, P., Sacramento, J., Saxe, A., Scellier, B., Schapiro, A. C., Senn, W., Wayne, G., Yamins, D., Zenke, F., Zylberberg, J., Therien, D., and Kording, K. P. (2019). A deep learning framework for neuroscience. *Nature Neuroscience*, 22(11):1761–1770.

[Schaefer et al., 2022] Schaefer, S., Gehrig, D., and Scaramuzza, D. (2022). AEGNN: Asynchronous event-based graph neural networks. *IEEE Conference on Computer Vision and Pattern Recognition (CVPR)*.

[Schoenberg, 1948] Schoenberg, I. J. (1948). On variation-diminishing integral operators of the convolution type. *Proceedings of the National Academy of Sciences of the United States of America*, 34(4):164–169.

[Schuman et al., 2022] Schuman, C. D., Kulkarni, S. R., Parsa, M., Mitchell, J. P., Date, P., and Kay, B. (2022). Opportunities for neuromorphic computing algorithms and applications. *Nature Computational Science*, 2(11):10–19.

[Sherwood, 2013] Sherwood, W. E. (2013). *FitzHugh–Nagumo Model*, page 1–11. Springer, New York, NY.

[Sironi et al., 2018] Sironi, A., Brambilla, M., Bourdis, N., Lagorce, X., and Benosman, R. (2018). HATS: Histograms of averaged time surfaces for robust event-based object classification. In *2018 IEEE/CVF Conference on Computer Vision and Pattern Recognition*, pages 1731–1740.

[Soomro et al., 2012] Soomro, K., Zamir, A. R., and Shah, M. (2012). UCF101: A dataset of 101 human actions classes from videos in the wild. *ArXiv*, abs/1212.0402.

[Tayarani-Najaran and Schmuker, 2021] Tayarani-Najaran, M. and Schmuker, M. (2021). Event-based sensing and signal processing in the visual, auditory and olfactory domain: A review. *Frontiers in Neural Circuits*, 15.

[Theilman and Aimone, 2023] Theilman, B. H. and Aimone, J. B. (2023). Goemans-Williamson MAXCUT approximation algorithm on Loihi. In *Proceedings of the 2023 Annual Neuro-Inspired Computational Elements Conference*, NICE ’23, pages 1–5, New York, N. USA. Association for Computing Machinery.

[Uhr, 1972] Uhr, L. (1972). Layered ‘recognition cone’ networks that preprocess, classify and describe. *IEEE Trans. Comput.*, C-21:pp. 759–768.

[Voelker et al., 2019] Voelker, A., Kajic, I., and Eliasmith, C. (2019). Legendre memory units: Continuous-time representation in recurrent neural networks. *Neurips*.

[Witkin, 1987] Witkin, A. P. (1987). *Scale-Space Filtering*, pages 329–332. Morgan Kaufmann, San Francisco (CA).

[Worrall and Welling, 2019] Worrall, D. E. and Welling, M. (2019). Deep scale-spaces: Equivariance over scale. In *Neural Information Processing Systems*, volume 32.

[Zhao et al., 2015] Zhao, B., Ding, R., Chen, S., Linares-Barranco, B., and Tang, H. (2015). Feedforward categorization on aer motion events using cortex-like features in a spiking neural network. *IEEE Transactions on Neural Networks and Learning Systems*, 26(9):1963–1978.



(a) If $\phi : \mathcal{X} \rightarrow \mathcal{X}$ is covariant to the actions g and g' acting on some signal domain \mathcal{X} , then $g \cdot \phi = \phi' \cdot g'$, given some $x, x', x_\phi, x'_{\phi'} \in \mathcal{X}$.

(b) If $\phi : \mathcal{X} \rightarrow \mathcal{X}$ is invariant to the action g on some signal \mathcal{X} , then $\phi' \cdot g = \phi$, given some $x, x', x'' \in \mathcal{X}$.

Figure 11: Covariance (left) retains information about the actions g, g' after their application in some form, while invariance (right) discards it.

A Covariance properties in space and time

Definition A.1 (Covariance and invariance). Given a set \mathcal{X} , the map $\phi : \mathcal{X} \rightarrow \mathcal{X}$ is *covariant* if it obeys $\phi(g \cdot x) = g' \cdot \phi(x)$ for all actions g, g' over \mathcal{X} . That is, there is a sense in which the map ϕ applied *before* the group action is comparable to its application *after* the group action. This is also known as *equivariance*. If g acts *trivially* on \mathcal{X} , then $\phi(g \cdot x) = \phi(1 \cdot x) = \phi(x) = 1(\phi \cdot x) = g(\phi \cdot x)$ and we call ϕ *invariant* to g .

Definition A.2 (Translation). A shift operation ($\phi_{translate}$) translates a signal x by a translation offset Δx according to $(\Delta x, x) = x - \Delta x$.

Definition A.3 (Scaling). The scaling operation (ϕ_{scale}) scales a signal x by a spatial scaling factor s defined by $(s, x) = sx$.

Definition A.4 (Rotation). Rotations rotate a signal x around its origin by an angle θ . In two dimensions, when $x \in \mathbb{R}^2$, we describe this in matrix form

$$(\theta, x) = \left(\theta, \begin{bmatrix} x_1 \\ x_2 \end{bmatrix} \right) = \begin{bmatrix} \cos \theta & -\sin \theta \\ \sin \theta & \cos \theta \end{bmatrix} \begin{bmatrix} x_1 \\ x_2 \end{bmatrix} \quad (35)$$

Definition A.5 (Shearing). The shear operation (ϕ_{shear}) translates a signal x parallel to a given line. In two dimensions, the shear operation (λ, x) can be defined using the shear matrix parallel to either the horizontal

$$(\lambda_x, x) = \left((\lambda_x, 0), \begin{bmatrix} x_1 \\ x_2 \end{bmatrix} \right) = \begin{bmatrix} 1 & \lambda_x \\ 0 & 1 \end{bmatrix} \begin{bmatrix} x_1 \\ x_2 \end{bmatrix} \quad (36)$$

or vertical

$$(\lambda_y, x) = \left((0, \lambda_y), \begin{bmatrix} x_1 \\ x_2 \end{bmatrix} \right) = \begin{bmatrix} 1 & 0 \\ \lambda_y & 1 \end{bmatrix} \begin{bmatrix} x_1 \\ x_2 \end{bmatrix} \quad (37)$$

axis.

Definition A.6 (Affine transformation). We define an affine transformation as any map $\psi : \mathcal{V} \mapsto \mathcal{V}$ that sends a point in a vector space \mathcal{V} to another point in that same vector space. Affine transformations are the most general type of linear transformation, and include arbitrary compositions of translations, scalings, rotations, and shearings. For image transformations in two dimensions, an affine transformation in matrix form (\mathcal{A}) is given by

$$(\mathcal{A}, x) = \left(\mathcal{A}, \begin{bmatrix} x_1 \\ x_2 \end{bmatrix} \right) = \begin{bmatrix} a_{11} & a_{12} \\ a_{21} & a_{22} \end{bmatrix} \begin{bmatrix} x_1 \\ x_2 \end{bmatrix} \quad (38)$$

Definition A.7 (Galilean transformation). Newtonian physics tells us that two reference frames with an N -dimensional spatial component ($x \in \mathbb{R}^N$) and temporal component ($t \in \mathbb{R}$) are related according to

$$\begin{aligned} x' &= x + vt \\ t' &= t \end{aligned} \quad (39)$$

where v is the relative velocity for each dimension $n \in N$. In the case of two spatial dimensions ($n = 2$) and one temporal dimension, we describe the relationship between two points p in space-time as follows [Lindeberg, 2023a, Eq. (20)]

$$(v, p') = \begin{bmatrix} x'_1 \\ x'_2 \\ t' \end{bmatrix} = \begin{bmatrix} 1 & 0 & v_1 \\ 0 & 1 & v_2 \\ 0 & 0 & 1 \end{bmatrix} \begin{bmatrix} x_1 \\ x_2 \\ t \end{bmatrix} = G p \quad (40)$$

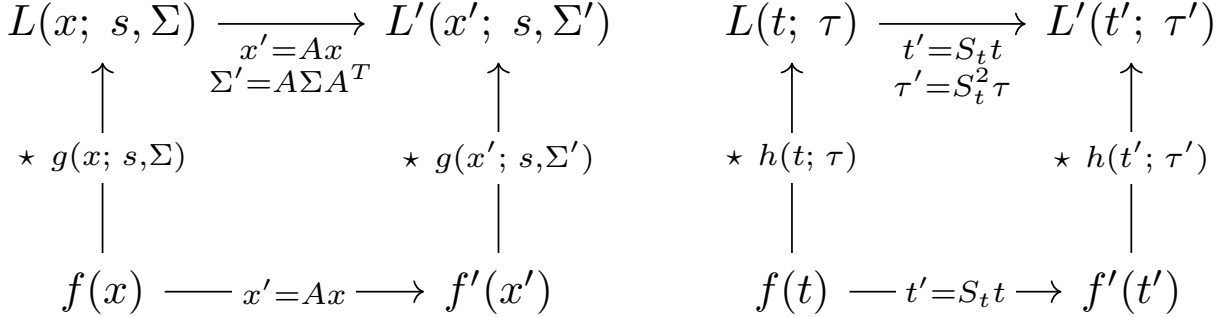


Figure 12: The relation of a signal (f) and its scale-space representation (L) under spatial affine transformations (left) and temporal scaling transformations (right).

Following the above definitions of covariance and transformations, we distinguish between invariance as well as covariance properties for affine *spatial* transformations, *temporal* scaling, and *spatio-temporal* Galilean transformations.

B Covariance properties in scale-space representations

Scale-space theory provides a means to represent signals at varying spatial or temporal scales. The covariance properties of the scale-space representations arrive from the commutative relationships shown in Figure 12, which we will elaborate and expand below. Given a continuous signal $f(t): \mathbb{R} \rightarrow \mathbb{R}$, we define the scale-dependent scale-space representation L , parameterized by a scale $\tau \in \mathbb{R}_+$: $L_g(t, \tau)$, as the convolution integral with scale-dependent kernels $g: \mathbb{R} \times \mathbb{R}_+ \rightarrow \mathbb{R}$ [Lindeberg, 2023b]

$$L_g(t, \tau) = g(t) \star f(t) = (g \star f)(t) = \int_{-\infty}^{\infty} g(\xi; \tau) f(t - \xi) d\xi \quad (41)$$

For this property to hold, the kernel g must *retain or diminish* variations, such that the changes in sign values for any signal sequence following the kernel application is less than or equal to the number of changes in sign value before that kernel has been applied. Specifically, if we, following Schoenberg [Schoenberg, 1948], define a “sign change detection function” $V: (\mathbb{R} \rightarrow \mathbb{R}) \rightarrow \mathbb{N}$, that finds the number of times a function f changes sign given the sequence $\{f(t_0), f(t_1), \dots, f(t_n)\}$, and require that

$$V(g \star f) \leq V(f) \quad (42)$$

This condition is met if and only if h has a bilateral Laplace transform of the form

$$\int_{-\infty}^{\infty} e^{-st} g(t) dt = C e^{\gamma s^2 + \delta s} \prod_{i=1}^{\infty} \frac{e^{a_i s}}{1 + a_i s} \quad (43)$$

for $-c < \text{Re}(s) < c$, $c > 0$, $\gamma \geq 0$, $C \neq 0$, δ, a_i are real, and assuming $\sum_{i=1}^{\infty} a_i^2$ converges [Schoenberg, 1948]. Over the spatial domain, the Gaussian kernel for some signal x and covariance matrix Σ

$$g(x; \Sigma) = \frac{1}{2\pi \sqrt{\det \Sigma}} e^{-x^T \Sigma^{-1} x / 2} \quad (44)$$

along with its derivatives, is known to meet the above conditions [Lindeberg, 1994]. Concerning the temporal domain, it was shown by Lindeberg and Fagerström [Lindeberg and Fagerström, 1996] that if we require the temporal kernels to be time-causal, in the sense that they do not access values from the future in relation to any time moment, then convolutions with truncated exponential kernels [Lindeberg, 2023b, Eq. (8)]

$$h_{\text{composed}}(\cdot; \mu) = *_{k=1}^K h_{\text{exp}}(\cdot; \mu_k) \quad (45)$$

by both necessity and sufficiency constitute the class of time-causal temporal scale-space kernels.

B.1 Temporal scale covariance for the causal limit kernel

The Gaussian kernel does not immediately apply to the temporal domain because it relies on future, unseen, signals, which is impossible in practice [Koenderink, 1988]. Instead, based on the above cited classification of time-causal

scale-space kernels [Lindeberg and Fagerström, 1996, Lindeberg, 2016, Lindeberg, 2023b], convolutions with truncated exponential kernels h_{exp}

$$h_{exp}(t, \mu_k) = \begin{cases} \frac{1}{\mu_k} e^{-t/\mu_k} & t > 0 \\ 0 & t \leq 0 \end{cases} \quad (46)$$

coupled in cascade, where μ_k are temporal time constants, lead to the formulation of a temporal scale-space representation.

Note that we assume normalization, such that $\int_{-\infty}^{\infty} h(t; \tau) dt = 1$. By composing K truncated exponential kernels in cascade, in the limit when K trends to ∞ , Lindeberg [Lindeberg, 2016, Eq. (38)] introduces a “limit kernel” $\hat{\Psi}$ in the Fourier domain

$$\begin{aligned} \hat{\Psi}(\omega; \tau, c) &= \lim_{K \rightarrow \infty} \hat{h}(\omega; \tau, c, K) \\ &= \prod_{k=1}^{\infty} \frac{1}{1 + ic^{-k} \sqrt{c^2 - 1} \sqrt{\tau} \omega} \end{aligned} \quad (47)$$

where the temporal scaling parameter, τ_k for $k \in K$ scale levels, is distributed according to integer powers of the distribution parameter c following $\tau_k = c^{2(k-K)} \tau$ for $c > 1$. Scaling $\hat{\Psi}$ with some factor S_t (t denoting time), we see that [Lindeberg, 2016, Eq. (43)]

$$\begin{aligned} \hat{\Psi}\left(\frac{\omega}{S_t}; S_t^2 \tau, c\right) &= \prod_{k=1}^{\infty} \frac{1}{1 + ic^{-k} \sqrt{c^2 - 1} \sqrt{S_t^2 \tau} \frac{\omega}{S_t}} \\ &= \hat{\Psi}(\omega; \tau, c) \end{aligned} \quad (48)$$

The scale-space representation of a given signal f by a scaling factor $S_t = 1/c$ such that $t' = t/c$ and $\tau' = \tau/c^2$ is then [Lindeberg, 2016, Eq. (45)]

$$L'(t'; \tau', c) = \left(\Psi\left(\cdot; \frac{\tau}{c^2}, c\right) \star f'(\cdot) \right) (t'; \tau' -, c) \quad (49)$$

Covariance between smoothing representations L and L' follows, again under logarithmic distribution of scales

$$L(t; \tau, c) = L'(t'; \tau', c) \quad \text{for } t' = c^j t \text{ and } \tau' = c^{2j} \tau \quad (50)$$

where τ is the *temporal* scale and S_t denotes a temporal rescaling factor $S_t = c^j, j \in \mathbb{Z}$. Returning to the temporal domain, this implies a direct relationship between neighboring temporal scales [Lindeberg, 2023a, Eq. (41)]

$$\Psi(t; \tau, c) = h\left(t; \frac{\sqrt{c^2 - 1}}{c} \sqrt{\tau}\right) \star \Psi\left(\cdot; \frac{\tau}{c^2}, c\right) \quad (51)$$

with the following scaling property

$$S\Psi(S_t t; S_t^2 \tau, c) = \Psi(t; \tau', c) \quad (52)$$

Ψ can be understood as a *scale-covariant time-causal limit kernel*, because it “obeys a closedness property over all temporal scaling transformations $t' = c/t$ with temporal rescaling factors $S = c^j$ ($j \in \mathbb{Z}$) that are integer powers of the distribution parameter c ” [Lindeberg, 2023a, p. 10].

B.2 Covariance over joint spatial and temporal transformations

We now want to derive a single kernel that is provably covariant to spatial affine and Galilean transformations as well as temporal scaling transformations. With the addition of time, the spatial and temporal signals are no longer separable. Instead, we look to Newtonian physics, where relative motions between two frames of reference are described by Galilean transformations according to (39). Directly building on the (spatial) Gaussian kernel (44) and the time-causal limit kernel (51), we can, following [Lindeberg, 2016], establish spatio-temporal receptive fields as their composition

$$T(x, t; \Sigma, v, \tau, c) = g(x; \Sigma) \Psi(t; \tau, c) \quad (53)$$

The corresponding scale-space representation is

$$L(x, t; \Sigma, v, \tau, c) = \iint_{\xi \in \mathbb{R}^2} \int_{\rho \in \mathbb{R}} T(\xi, \rho; \Sigma, v, \tau, c) f(x - \xi, t - \rho) d\xi d\rho \quad (54)$$

Consider two spatio-temporal signals (video sequences) f, f' that are related according to a spatial affine transformation, a Galilean spatio-temporal transformation, and a temporal scaling transformation as follows

$$x' = A(x + wt) \quad \text{and} \quad (55)$$

$$t' = S_t t \quad (56)$$

According to Equation 21 in the main text

$$\Sigma' = A \Sigma A^T \quad (57)$$

we have

$$\begin{aligned} \Sigma'^{-1} &= (A \Sigma A^T)^{-1} = A^{-T} \Sigma^{-1} A^{-1} \quad \text{and} \\ \det \Sigma' &= \det(A \Sigma A^T) = |\det A|^2 \det \Sigma \end{aligned} \quad (58)$$

If we further set the relationships of two signals subject to Galilean and affine transformations as follows

$$\begin{aligned} v &= -A^{-1}w + A^{-1}v' S_t \\ Av &= -w + v' S_t \\ v' &= (Av + w)/S_t \end{aligned} \quad (59)$$

we can rewrite the Gaussian kernel (44) under Galilean and affine transformations as

$$\begin{aligned} g(x' - v't'; \Sigma') &= \frac{1}{2\pi\sqrt{\det \Sigma'}} \exp\left\{(-(x' - v't')^T \Sigma'^{-1} (x' - v't')/2)\right\} \\ &= \frac{1}{2\pi|\det A|\sqrt{\det \Sigma}} \exp\left(-(A(x + wt) - ((Av + w)/S_t)S_t t)^T A^{-T} \right. \\ &\quad \left. \Sigma^{-1} A^{-1} (A(x + wt) - ((Av + w)/S_t)S_t)/2\right) \\ &= \frac{1}{2\pi|\det A|\sqrt{\det \Sigma}} \exp\left(-(x - vt)^T \Sigma^{-1} (x - vt)/2\right) \end{aligned} \quad (60)$$

For f' we have the corresponding spatio-temporal scale-space representation as in (54)

$$L'(x', t'; \Sigma', v', \tau', v') = \iint_{\xi' \in \mathbb{R}^2} \int_{\rho' \in \mathbb{R}} T'(\xi', \rho'; \Sigma', v', \tau', c') f'(x' - \xi', t' - \rho') d\xi' d\rho' \quad (61)$$

We now exchange variables according to (55) and (56) to find

$$\begin{aligned} d\xi' &= |\det A| d\xi \\ d\rho' &= S_t d\rho \end{aligned} \quad (62)$$

and, therefore,

$$\begin{aligned} L'(x', t'; \Sigma', v', \tau', v') &= \iint_{\xi' \in \mathbb{R}^2} \int_{\rho' \in \mathbb{R}} T'(\xi', \rho'; \Sigma', v', \tau', c') f'(x' - \xi', t' - \rho') d\xi' d\rho' \\ &= \iint_{\xi \in \mathbb{R}^2} \int_{\rho \in \mathbb{R}} T(\xi, \rho; \Sigma, v, \tau, c) f(x - \xi, t - \rho) d\xi d\rho \\ &= L(x, t; \Sigma, v, \tau, v) \end{aligned} \quad (63)$$

which establishes the desired covariance property for the spatio-temporal scale-space representation L under affine, Galilean, and temporal scaling transformations, as shown in Figure 1 in the main text. This result also holds for the temporal Gaussian kernel (44) or truncated exponential kernel (46) by relating $\tau' = S_t^2 \tau$.

B.3 Temporal scale covariance for parallel first-order integrators

Consider a parallel set of temporal K scale channels with a single time constant for each parallel timescale “channel”, modelled as a truncated exponential kernel as in equation (46):

$$h_{composed}(\cdot; \tau_k) = h_{exp}(\cdot; \mu_k) \quad (64)$$

for $\mu_k = \sqrt{\tau_k}$ [Lindeberg, 2013, Eq. (16)] Each “channel” would assign a unique temporal scale-representation of the initial signal with a delay and duration, parameterized by μ_k . We denote a temporal scale-space channel representation T for some signal $f: \mathcal{X} \rightarrow \mathcal{X}$

$$T(t; \mu) = \int_{u=0}^{\infty} f(t-u) h_{exp}(u; \mu) du \quad (65)$$

and observe the direct relation under a temporal scaling operation $t' = St$ for two functions $f'(t') = f(t)$

$$\begin{aligned} T(t'; \mu') &= \int_{u'=0}^{\infty} f'(t' - u') \frac{1}{\mu'} e^{-t'/\mu'} du' \\ &\stackrel{(1)}{=} \int_{u=0}^{\infty} f'(S(t-u)) \frac{1}{S\mu} e^{-St/S\mu} S du \\ &= \int_{u=0}^{\infty} f(t-u) \frac{1}{\mu} e^{-t/\mu} du \\ &= T(t; \mu) \end{aligned} \quad (66)$$

where step (1) sets $u' = Su$, $du' = Sdu$, and $\mu' = S\mu$. A single filter T is thus scale-covariant for the scaling operation S , and a *set* of filters ($h_{composed}$) will be scale-covariant over multiple scales, provided the logarithmic distribution of K scales μ_k as in equation (50), and for scaling factors S that are integer powers of the ratio between the time constants μ_k of adjacent scale levels.

C Temporal scale covariance for leaky integrators

This section establishes temporal scale covariance for leaky integrators by demonstrating that they are special cases of a first-order integrator, after which the temporal scale covariance guarantees for first-order integrators apply, as in Section B.3.

A linear leaky integrator describes the evolution of a voltage u characterized by the following first-order integrator

$$\mu \frac{du}{dt} = -(u - u_0) + RI \quad (67)$$

where μ is a time constant controlling the speed of the integration, u_0 is the “resting state”, or target value of the neuron it will leak towards, R is a linear resistor, and I describes the driving current [Gerstner et al., 2014]. Assuming $u_0 = 0$ and $R = 1$ we arrive at [Gerstner et al., 2014, Eliasmith and Anderson, 2004]

$$u(t; \mu) = \frac{1}{\mu} \int_0^{\infty} e^{-\xi/\mu} I(t - \xi) d\xi \quad (68)$$

This is precisely the first-order integrator in the form of equation (46), and the temporal scale covariance from equation (66) follows.

D Temporal scale covariance for thresholded leaky integrators

This section establishes temporal scale covariance for thresholded linear leaky integrators. We first establish the usual, discrete formulation of thresholded leaky integrator-and-fire models and later introduce the spike response model that generalizes the neuron model as a set of connected filters. Finally, we build on the proof for the causal first-order leaky integrator above to establish temporal scale covariance for leaky integrate-and-fire models.

The leaky integrate-and-fire model is essentially a leaky integrator with an added threshold [Gerstner et al., 2014], which discretizes the activation using the Heaviside function H

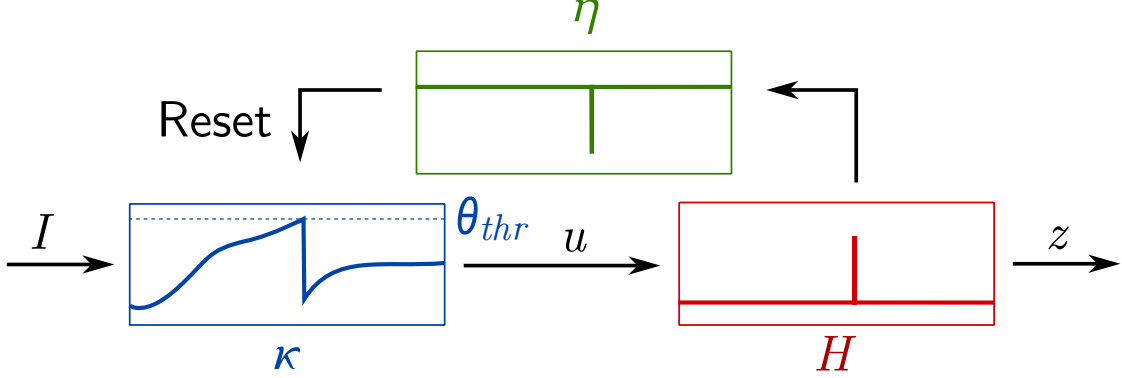


Figure 13: The spike response model recasts the leaky integrate-and-fire model as a composition of three filters: a membrane filter in blue (κ), a threshold filter in red (H), and a reset filter in green (η). The graphs inside the filters depict their respective outputs over time using the kernels in (74), given some input signal, I .

$$H(x; \theta_{thr}) = \begin{cases} 1, & x \geq \theta_{thr} \\ 0, & x < \theta_{thr} \end{cases} \quad (69)$$

parameterized over some threshold value θ_{thr} . When $H = 1$, we say that the neuron “fires”, whereupon the integrated voltage (its membrane potential) resets to θ_{reset} :

$$u(t; \mu) = \theta_{reset} \quad (70)$$

The total dynamics of the leaky integrate-and-fire neuron model can be summarized as three equations capturing the subthreshold dynamic from equation (68), the thresholding from equation (69), and the reset from equation (70) [Gerstner et al., 2014].

It is worth noting that the threshold in the continuous case is a simplification of the dirac delta function defined as

$$\delta(t) = \lim_{\sigma \rightarrow 0} g(t; \sigma) \quad (71)$$

where g is a normalized Gaussian kernel. Integrating over time, we therefore have

$$\int_{-\infty}^{\infty} \delta(t) dt = 1 \quad (72)$$

Hence the “spike” ($H = 1$) in equation (69): any layer following a thresholded activation function will be subject to a series of these unit impulses over time. As such, the neuron activation output function can be written as a sum of N unit impulses over time [Gerstner et al., 2014]

$$\Gamma(t) = \sum_{n=1}^N \delta(t - t_n) \quad (73)$$

D.1 Spike response model

This formulation generalizes to numerous neuron models, but we will restrict ourselves to the LIF equations, which can be viewed as a composition of three filters: a membrane filter (κ), a threshold filter (H), and a membrane reset filter (η') shown in Figure 13. The spike response model defines neuron models as a composition of parametric functions (filters) of time [Gerstner et al., 2014]. The membrane filter and membrane reset filter describes the subthreshold dynamics as follows:

$$u(t) = \int_0^{\infty} \eta'(s) \Gamma(t-s) + \kappa(s) I(t-s) ds \quad (74)$$

The reset filter, η' , can be understood as the resetting mechanism of the neuron, that is, the function controlling the subthreshold behaviour immediately after a spike. This contrasts the LIF formalism from equation (70) because the resetting mechanism is now a function of time instead of a constant.

Since the resetting mechanism depends entirely on the time of the threshold activations, we can recast it to a function of time (t), where t_f denotes the time of the previous spike

$$u(t) = \eta(t - t_f) + \int_0^\infty \kappa(s) I(t - s) ds \quad (75)$$

Following [Gerstner et al., 2014, Eq. (6.33)] we define η more concretely as a linearized reset mechanism for the LIF model

$$\eta(t - t_f; \mu_r) = -\theta_{thr} e^{-(t-t_f)/\mu_r} \quad (76)$$

The above equation illustrates how the “after-spike effect” decays at a rate determined by μ_r . Initially, the kernel corresponds to the *negative* value of θ_{thr} at the time of the spike, effectively resetting the membrane potential by θ_{thr} . In the LIF model, the reset is instantaneous, which we observe when $\mu_r \rightarrow 0$. This is visualized in Figure 13 where the set of filters correspond to the subthreshold mechanism in equation (68) (which we know to be scale covariant from equations (66)), the Heaviside threshold in equation (69), and the reset mechanism in equation (76).

We arrive at the following expression for the subthreshold voltage dynamics of the LIF model:

$$z(t) = -\theta_{thr} e^{-(t-t_f)/\mu_r} + \int_0^\infty \kappa(s) I(t - s) ds \quad (77)$$

D.2 Temporal covariance for the LIF model

We are now ready to state the scale-space representation T of a LIF model as a special case of the above equation (77) where $\kappa := h_{exp}$:

$$T(t; \mu, \mu_r) = -\theta_{thr} e^{-(t-t_f)/\mu_r} + \int_0^\infty f(t - z) h_{exp}(z; \mu) dz \quad (78)$$

Considering a temporal scaling operations $t' = St$ and $t'_f = St'_f$ for the functions $f'(t') = f(t)$, we follow the steps in equation (66):

$$\begin{aligned} T(t'; \mu', \mu'_r) &= -\theta_{thr} e^{-(t'-t'_f)/\mu'_r} + \int_{z'=0}^\infty f'(t' - z') \frac{1}{\mu'} e^{-t'/\mu'} dz' \\ &\stackrel{(1)}{=} -\theta_{thr} e^{-S(t-t_f)/S\mu'_r} + \int_{z=0}^\infty f'(S(t - z)) \frac{1}{S\mu} e^{-St/S\mu} S dz \\ &= -\theta_{thr} e^{-(t-t_f)/\mu_r} + \int_{z=0}^\infty f(t - z) \frac{1}{\mu} e^{-t/\mu} dz \\ &= T(t; \mu, \mu_r) \end{aligned} \quad (79)$$

where step (1) sets $z' = Sz$, $dz' = Sdz$, $\mu' = S\mu$, and $\mu'_r = S\mu_r$. This concludes the proof that the LIF model, described as a set of linear filters, retains temporal scale covariance.

E Training setup

The model is implemented using the Norse library [Pehle and Pedersen, 2021] and trained on a dataset generated with the Generated Event Response Data (GERD) framework [Pedersen et al., 2024b]. The leaky integrator and leaky integrate-and-fire models are trained on NVIDIA A100 GPUs due to the high memory requirements, while the ReLU models are trained on NVIDIA V100 and 4090 cards. The models are trained using the Adam optimizer [Kingma and Ba, 2014] with a learning rate of 5×10^{-4} . The batch sizes vary to account for the differing memory requirements. Each model is trained for 50 epochs and repeated 5 times.

All the initialization code and hyperparameters are available for reproduction at <https://jegp.github.io/nrf>.

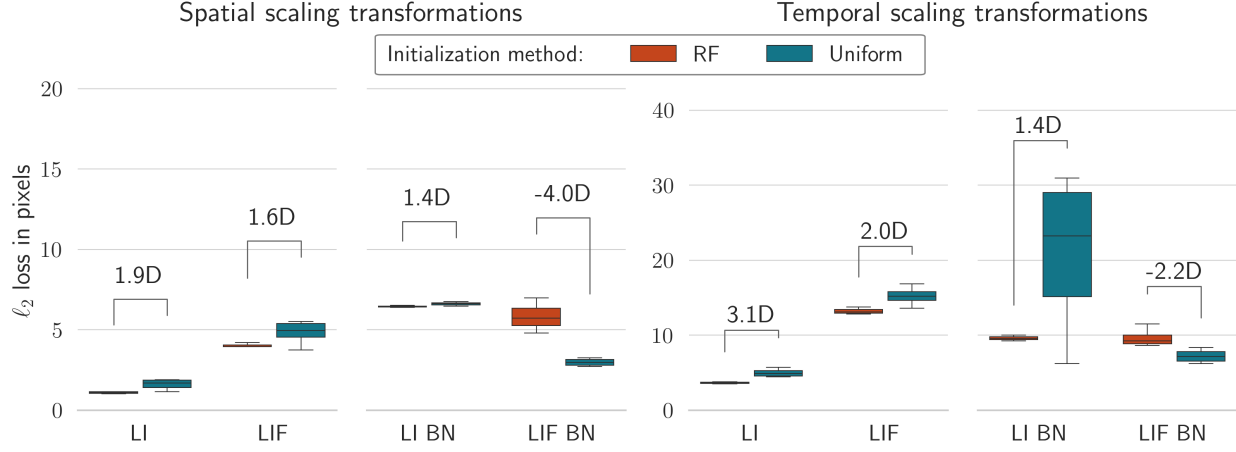


Figure 14: Results of the spatial and temporal scaling experiments with and without batch normalization (BN). As in the main text, the model parameters are either initialized according to the spatio-temporal receptive fields or sampled uniformly.

F Effects of batch normalization

To explore the hypothesis about the normalizing effect of the receptive field, a copy of the model presented in the main text was constructed with added batch normalization layers. Batch normalization normalizes signals with the following transformation [Ioffe and Szegedy, 2015]

$$\hat{x} = \frac{x_k - \mathbb{E}[x_k]}{\sqrt{\text{Var}[x_k]}} \gamma + \beta \quad (80)$$

where $\mathbb{E}[x_k]$ and $\text{Var}[x_k]$ are the mean and variance of the k -th feature, respectively, and γ and β are learnable parameters.

Layers following batch normalization are known to be less sensitive to distributional shifts both from the input data and the parameter changes [Ioffe and Szegedy, 2015]. Theoretically, this makes the model generalize better to unseen data and accelerate training at the cost of computational overhead. This overlaps partly with the theoretical properties of the scale-space representation, since they exhibit transformational covariance and improved generalization.

The addition of batch normalization could hypothetically cancel out some benefits of the scale-space initialization, as it would normalize the signals and provide part of the generalization properties. Figure 14 shows the comparison between models initialized with the spatio-temporal receptive fields and models initialized uniformly, this time with added batch normalization before each temporal activation layer in the blocks. Compared to the results in the main text, initialization with spatio-temporal receptive fields show significantly less improvement compared to the uniform initialization. In fact, for the spiking neuron models, it even hurts the performance. This is likely due to the fact that constant normalization reduces the sensitivity around the firing threshold, which risks silencing the neuron and quenching the gradients, thus leading to a less effective training.

However, batch normalization is not compatible with neuromorphic architectures, since batch normalization operation in (80) requires the synchronous computation of the mean and variance over the entire batch. As such, the comparison is a purely theoretical inquiry into the effects of the scale-space initialization.